



**HAL**  
open science

# Highlighting the impact of the construction history of a Cultural Heritage building through a vibration-based Finite Element model updated by Particle Swarm Algorithm

Arnaud Montabert, E. Diego Mercerat, H el ene Lyon-Caen, Maria Lancieri

## ► To cite this version:

Arnaud Montabert, E. Diego Mercerat, H el ene Lyon-Caen, Maria Lancieri. Highlighting the impact of the construction history of a Cultural Heritage building through a vibration-based Finite Element model updated by Particle Swarm Algorithm. *International Journal of Architectural Heritage*, In press, 10.1080/15583058.2023.2219237 . hal-04133213v1

**HAL Id: hal-04133213**

**<https://hal.science/hal-04133213v1>**

Submitted on 19 Jun 2023 (v1), last revised 24 Jul 2023 (v2)

**HAL** is a multi-disciplinary open access archive for the deposit and dissemination of scientific research documents, whether they are published or not. The documents may come from teaching and research institutions in France or abroad, or from public or private research centers.

L'archive ouverte pluridisciplinaire **HAL**, est destin ee au d ep ot et  a la diffusion de documents scientifiques de niveau recherche, publi es ou non,  emanant des  tablissements d'enseignement et de recherche fran ais ou  trangers, des laboratoires publics ou priv es.

Public Domain

# Highlighting the impact of the construction history of a Cultural Heritage building through a vibration-based Finite Element model updated by Particle Swarm Algorithm

Arnaud MONTABERT <sup>\*1, 3, 4</sup>, E. Diego MERCERAT<sup>2</sup>, H el ene LYON-CAEN<sup>1</sup>, and Maria LANCIERI<sup>3</sup>

<sup>1</sup>Ecole Normale Sup erieure, PSL University, CNRS, U.M.R.8538-Laboratoire de G eologie, 24 Rue Lhomond, 75005 Paris, France

<sup>2</sup>Equipe REPSODY, CEREMA M editerran ee, 06903, Sophia Antipolis, 500 route des Lucioles, France.

<sup>3</sup>Institut de Radioprotection et de S uret e Nucl eaire (IRSN), PSE-ENV/SCAN/BERSIN, 31, avenue de la Division Leclerc, BP 17, 92262 Fontenay-aux-Roses, CEDEX, France

<sup>4</sup>Universit e Paris-Saclay, CentraleSup elec, ENS Paris-Saclay, CNRS, Laboratoire de M ecanique Paris-Saclay, 91190, Gif-sur-Yvette, France.

---

## Abstract

Numerical models play a primary role in Cultural Heritage preservation. Nevertheless, the design of a realistic model remains challenging due not only to the complex behavior of masonry but also to the asynchronous building phases, the damage induced by natural and anthropic aggression, and the associated repairs. This paper discusses the impact of the information provided by an in-depth analysis of the construction history on the updating process of a Finite Element building model. The case study is the church of Sant'Agata del Mugello (Italy); for this building, a previous historical-archaeological study identified and recorded the asynchronous construction phases, the repair techniques, and the damage induced by three historical earthquakes (1542, 1611, and 1919)—moreover, a dense ambient vibration survey allowed to identify the modal parameters. The information from previous works is summarized in five Finite Element models with increasing complexity. A vibration-based model updating methodology based on a Particle Swarm Algorithm is developed. This work shows that the best minimization of the difference between the numerical and experimental modal parameters is obtained with the numerical model considering the identified construction techniques, repair phases, and connection relations between the bell tower and the nave.

**Keywords** : *Cultural Heritage, construction history, masonry church, vibration-based model updating, Operational Modal Analysis, Particle Swarm Optimization, objective function, building techniques, Sant'Agata del Mugello.*

## Highlights

- Using the construction history and the stratigraphic analysis to better constrain the vibration-based model updating of the church of the Sant'Agata del Mugello;
- Use of a Particle Swarm Algorithm to update material parameters and lateral stiffness.

---

Received 28 October 2022; Accepted 24 May 2023 for publication in International Journal of Architectural Heritage. Manuscript DOI: 10.1080/15583058.2023.2219237

\*Corresponding author presently working at: Universit e Paris-Saclay, CentraleSup elec, ENS Paris-Saclay, CNRS, Laboratoire de M ecanique Paris-Saclay, 91190, Gif-sur-Yvette, France. E-mail addresses : arnaud.montabert@ens-paris-saclay.fr

# 1 Introduction

Finite element (FE) model updating is an essential step in structural engineering before any further prediction. It aims to evaluate unknown model parameters (material properties and boundary conditions) by minimizing the discrepancy between observable and predicted dynamic parameters. Solving this inverse problem consists of three main steps ([Tarantola 1987](#)) :

- Step 1 : Parameterization of the system by identifying a minimal set of model parameters characterizing the system (elastic moduli, mass density, etc.),
- Step 2 : Forward modeling using a mathematical model allowing for given values of model parameters to make some predictions on the results of observable parameters
- Step 3 : Identification of a relevant objective function to minimize the discrepancy between observable and predicted parameters.

Applying this framework to the model updating of Cultural Heritage buildings is challenging due to the low degree of knowledge compared to the high complexity of the structure (geometry, nonlinear behavior of masonry, heterogeneities of masonry, aged material, and complex construction history). It impacts the three steps of the inverse problem process. In recent decades, guidelines such as [ICOMOS 2003](#) ; [Direttiva del Presidente del Consiglio dei Ministri DPCM DPCM](#) have been designed as a first diagnosis phase to limit the degree of uncertainty of model parameters. Collecting information on the construction history helps identify the relevant set of model parameters that characterize the system and irregularities with neighboring buildings or between different parts of the building that constrain the boundary conditions (step 1). Characterizing the geometry through an on-site geometric survey (terrestrial laser scanner, photogrammetry, etc) and inspecting the overall state of the building provide valuable information to constrain the mesh and the constitutive laws used within the model. These input data are used to build a mathematical model to be improved, usually obtained by the finite element method (step 2 of the inverse problem process).

Natural frequencies and mode shapes (observable parameters) are obtained through Operational Modal Analysis (OMA), a classical non-invasive technique to guarantee the integrity of Cultural Heritage buildings. In vibration-based model updating (VBMU), these observable parameters are used to define the objective function (step 3). The literature shows that VBMU has been mainly applied to slender masonry buildings using a manual tuning technique to minimize the objective function since modal behavior is restricted to the main flexural and torsional modes of the slender structures (e.g., [Gentile and Saisi 2007](#), [Ramos et al. 2010](#), [Gentile et al. 2015](#), [Milani and Clementi 2021](#)).

Defining an objective function is a critical step in the VBMU process. Indeed, objective functions may be more or less sensitive to observable parameters, which favor local minima. Thus testing the sensitivity of several objective functions may be the first appropriate strategy, as it has been shown by [Limoge 2016](#). However, the analysis of more complex buildings (like an entire church) requires accounting for more complex modes that are difficult to fit using the ad-hoc techniques ([Limoge 2016](#), [Torres et al. 2017](#)). Increasing the complexity of the objective function and the number of local minima can lead to non-uniqueness and local minima. Additional information, like a rough characterization of model parameters, can help to discriminate between the candidate solutions. It is important to note that a direct characterization of the building material may not be feasible (even non-destructive) due to local authorities' rules. In this context, an appropriate sensitivity analysis of the model parameters and test of the different plausible objective functions is the only way to deal with ill-conditioned identification problems ( [Gentile et al. \(2015\)](#), [Salachoris et al. 2023](#)). On the other hand, several iterative optimization strategies to investigate the parameter space have been recently used ([Friswell and Mottershead 2013](#)). Among them, genetic algorithms (GA) and Particle Swarm Optimization (PSO) algorithms have been primarily used in recent years to overcome the nonlinear relationship between the global observable parameters obtained from vibration data and the model parameters. GA is the most used in the case of historic slender structure buildings (e.g. [Standoli et al. 2021](#) ; [Bianconi et al. 2020](#) ; [Jaishi and Ren 2007](#), [Salachoris et al. 2023](#)). Although results are pretty similar, the results of PSO and its computational efficiency are found to be better than GA, as the PSO carries out global and local searches simultaneously, whereas the GA concentrates specifically on global search ([Eberchart and Kennedy 1995](#) ; [Hassan et al. 2005](#) ; [Prashanth and Sujatha 2018](#)). Repeating the PSO process allows for testing the updating process's stability around an optimal solution and may be a promising alternative.

This paper applies the VBMU process to an entire medieval church with a complex building history. In particular, we propose highlighting the impact of the knowledge of the building history on the parametrization stage of the VBMU process (as recommended in the guidelines mentioned above). Indeed the detailed stratigraphic analysis

of a historical building reveals different phases of construction, thus going further than the simple diagnostics of identifying used materials.

Such a study can be conducted on a building where historical information is well known. For this reason, the church of Sant’Agata del Mugello was chosen as a case study since its construction history, and its modal parameters have been exhaustively described in previous works (Montabert et al. 2020; Montabert et al. 2022). Indeed, a cross-disciplinary approach combining a stratigraphic analysis of the church’s walls with information extracted from historical documents revealed the asynchronous construction of the church and numerous repairs associated with several historical earthquakes. We identified 12 building phases and 81 asynchronous repair units. Two dense OMA surveys identified ten modes. It has been shown that particularities of specific modes can be explained by events in the history of the building (damage associated with past earthquakes, repairs, and asynchronous construction, Montabert et al. 2022).

The VMBU of Sant’Agata is based on ad-hoc multiprocessing Particle Swarm Optimization.

A further challenge appears; indeed, the numerous information on this church (modal parameters and building history) rapidly increases the number of model parameters. A sensitivity analysis based on local perturbation is performed to test the relevance of each model parameter. PSO is repeated with an increasing number of particles to assess the stability of the solution.

The paper is structured as follows. The construction history of the church is first described. The results of the OMA are summarized. The methodology developed to update the FE model of Sant’Agata del Mugello is detailed. Five different Finite Element models with increasing complexity regarding constructive history are developed. The choice of model parameters, the sensitivity analysis, the definition of the objective functions, and the parameters of the PSO are discussed. The impact of the construction history is then discussed based on the results of the five optimization process.

## 2 The church of Sant’Agata del Mugello

### 2.1 Historical survey based on a cross-disciplinary approach

Sant’Agata del Mugello is a Romanesque church located in Northern Apennines in the intermontane Mugello basin (Tuscany, Italy). This area is characterized by moderate seismicity (Bonini et al. 2016); earthquake occurrences have been known at least since the middle of the 16th century. The largest known earthquakes occurred in 1542 (estimated M<sub>mw</sub><sup>1</sup> 6.0) and in 1919 (estimated M<sub>mw</sub> 6.4) (Rovida et al. 2016). In recent times, several seismic crises characterized by shallow earthquakes were recorded in 2008 and 2009 (Bonini et al. 2016) and more recently in 2019 with a maximum recorded magnitude of Mw 4.5 (Saccorotti et al. 2022). The Mugello seismicity deeply affected the building history of Sant’Agata, as shown in recent studies based on the combination of data found in archives, stratigraphic analysis, and an engineering diagnosis (Arrighetti 2015; Montabert et al. 2020). In particular, the stratigraphic analysis delineated the building phases by identifying the construction techniques used during different periods. 12 building phases were identified, claiming an asynchronous architectural evolution in geometry and material used. The main building phases are summarized below. Evidence point to the church’s existence at least since the 10th century. In the 15th century, the building was only composed of the nave and the central apse (phases 1, 2, and 3 in Fig. 1). During this century, the two side chapels were successively added (initial phase 3 of the lateral chapels in brown in Fig. 1), followed by the bell tower in a final stage (phase 4 of the bell tower in orange in Fig. 1-b-c-d). Phases 5 and 6 are related to minor renovations. The opening of a door in the east-facing wall of the bell tower in 1497 and the repair of the three windows of the southern wall of the nave correspond to phase 5. The rose window of the facade was repaired during phase 6 and is no longer there. The earthquake of June 6, 1542 (estimated macroseismic M<sub>mw</sub> 6.0, Rovida et al. 2016) induced much damage. The upper part of the bell tower collapsed, and cracks opened in the west and east wall of the bell tower throughout the total height. Only the south wall of the bell tower was rebuilt to its original height, changing the bell tower to a vertical L-shape tower (the rebuilt phase 7 of the bell tower is shown in green in Fig. 1-b-c-d, the L-shape at that time consisted of the orange and green part). The outer side of the facade, the north wall, and the south wall of the nave are still tilted. The two lateral chapels collapsed and are nowadays rebuilt using a different building technique (the rebuilt phase is shown in green in the two lateral chapels in Fig. 1-d). Phase 8 is related to minor repairs like filling openings in the nave or cracks in the bell tower. The earthquake of September 8, 1611 (estimated M<sub>mw</sub> 5.1) induced several cracks in the L-shape bell tower and weakened the upper part leading the bell tower to its current shape after a deep reconstruction (phase 9 shown in blue in Fig. 1-b-c-d). The 1919 earthquake (M<sub>mw</sub> 6.4) did not induce any damage, probably due to its greater epicentral distance. The door opened in the bell tower during phase 5 and was

---

1. M<sub>mw</sub> : Macroseismic Moment Magnitude

closed in phase 10. The arc of the central apse was raised about 1.20 m during phase 11. The rose window was filled in during phase 12. The final phase, 13, is related to all the restoration events during the 19th century.

Currently, the church can be subdivided into three main blocks : the bell tower, the nave, and a two-part block consisting of the central apse and the two lateral chapels (Fig. 1-a). A cloister was built near the southern facade of the church. Since the two buildings are in contact only in the southeast corner of the nave, highlighted by a thin wall, the cloister is not considered in this study (dotted lines in Fig. 1-a).

## 2.2 Geometrical and material survey

The geometry of the church is defined thanks to a Terrestrial Laser Scanner survey (TLS) conducted by the Department of Architecture at the University of Florence (Montabert et al. 2020). Thus, the church’s geometrical characteristics are extracted from the points cloud and summarized below.

The bell tower is 21 m high and almost squared base ( $6.3 \times 6.0 \text{ m}^2$ ). Its masonry walls are 1.10 m thick. The tower is composed of five floors.

The nave consists of a rectangular basement ( $15.7 \times 29.3 \text{ m}^2$ , Fig. 1). Its walls are about 0.80 m thick. The nave is covered by a timber frame whose beams are embedded in lateral walls. The central apse measures  $15.7 \times 29.3 \text{ m}^2$  (Fig. 1) and the two squared lateral chapels are  $4.4 \times 4.4 \text{ m}^2$  and  $4.5 \times 4.5 \text{ m}^2$  for the North and South chapel, respectively. A vault system overhangs the central apse and the two lateral chapels—their wall thickness range from 0.40 m to 0.70 m.

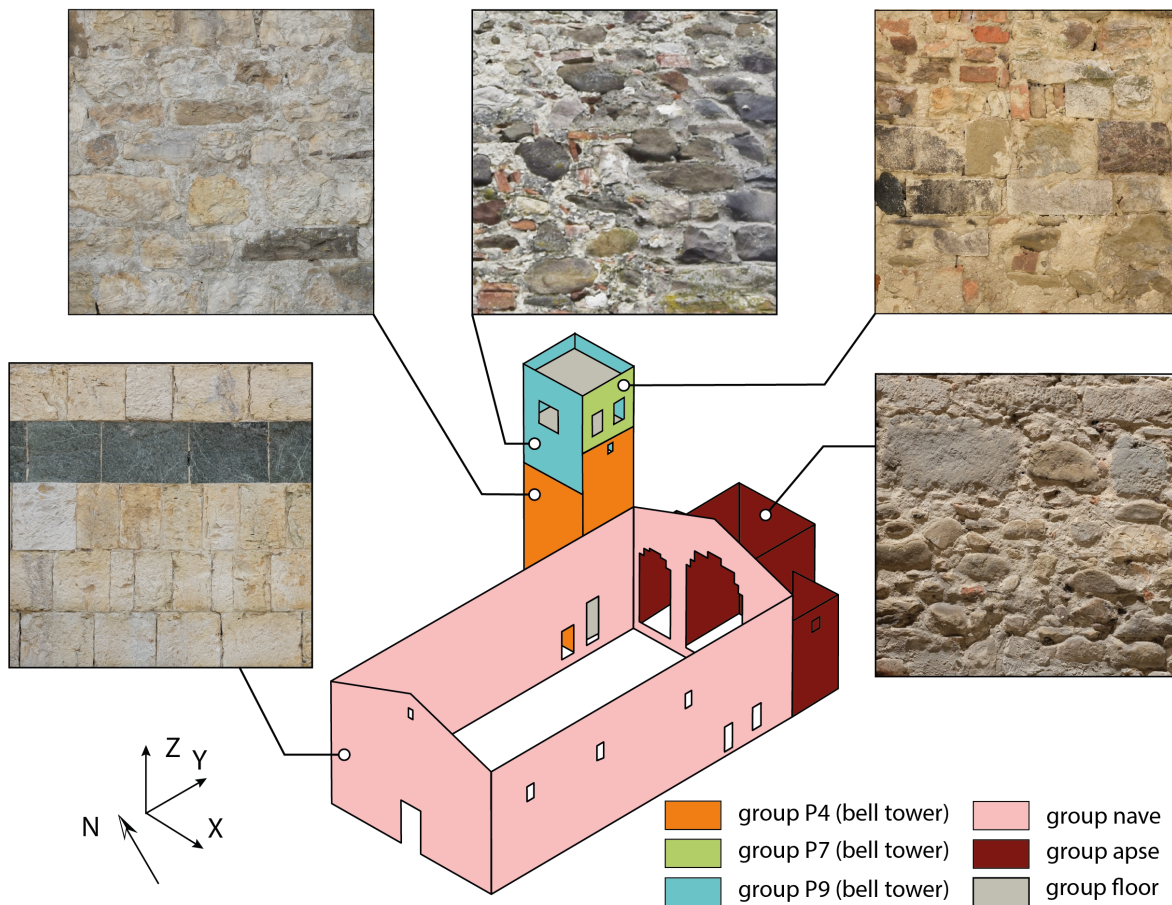


FIGURE 2 – Distribution of the main building techniques groups. Representative samples are 1 square meter (Montabert et al. (2020), Montabert (2021)).

The stratigraphic analysis conducted in previous work has demonstrated the use of 20 construction techniques and highlighted 81 repair units over the entire history of the church of Sant’Agata (Montabert et al. 2020). These construction techniques can, however, be grouped into five families detailed below (Fig. 2). Construction techniques identified in the nave consist mainly of using limestone blocks (Pietra Albarese) and little use of mortar identified

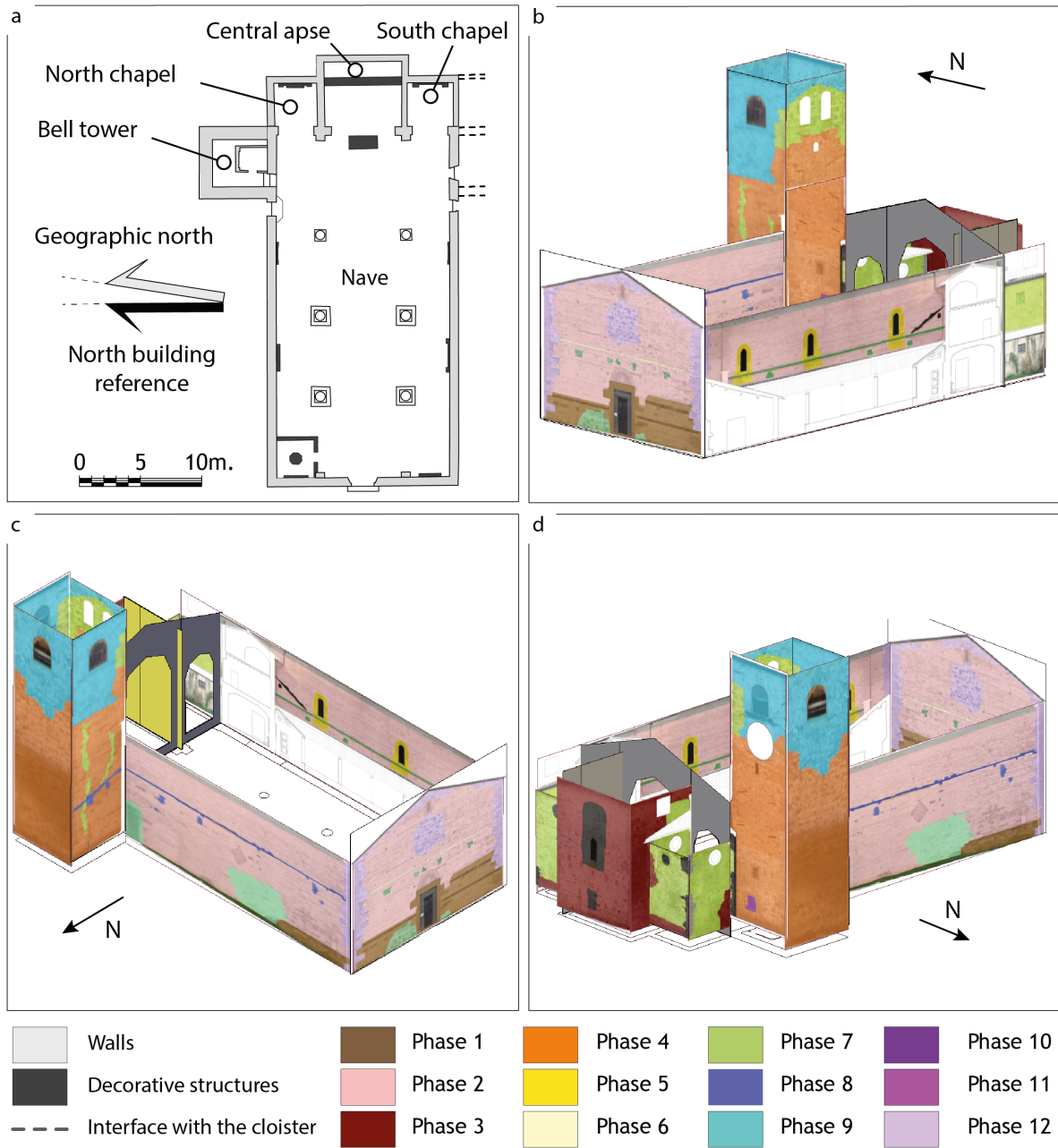


FIGURE 1 – a- Plan of the Sant'Agata del Mugello church. b-c-d 3D CAD-based model with the stratigraphic reading reported on orthophotos (based on [Montabert et al. \(2020\)](#), [Montabert \(2021\)](#)).

as a single constructive technique group *nave*. The masonry of the central apse and the two side-chapels identified as the group *apse* is composed of limestone rubble (Pietra Serena and Formazione di Silano) with a high proportion of mortar (joint  $\geq 2$  cm) and a small number of bricks.

Three distinct techniques composed the bell tower : group *tower-P4*, the group *tower-P7*, and group *tower-P9*, so-called in reference to their respective construction phase (phase 4, phase 7, and 9). The first group *tower-P4* comprises decimetric irregular blocks of hard limestone (Pietra Serena) bound with a competent mortar into a large joint ( $\geq 2$ cm). It corresponds to the initial phase of the bell tower.

The second group *tower-P7* is characterized by polymorphic limestone rubble, river pebbles, and a strong mortar presence. This technical group was used during the reconstruction of the bell tower after the 1542 earthquake phase 7 in Fig. 1). The third group *tower-P9* is composed of a mixture of limestone (Pietra Serena and Formazione di Silano), rubbles of different sizes, clay bricks, and massive use of mortar. The size of the blocks is smaller than in the other technical groups. This technical group was used to reconstruct the bell tower after the earthquake of 1611 (phase 9 in Fig. 1).

### 3 Operational Modal Analysis

Two dense Ambient Vibration Testing surveys were conducted in the church of Sant’Agata del Mugello and are described in previous work (Montabert et al. 2022). Vibrations were recorded at 81 nodes inside the nave, the apses, and the bell tower (the term node refers to the location of velocimeters). Two tri-axial velocimeters are used : 6 CMG40-T-1 (with a flat response between 0.2 Hz to 50 Hz) and 6 LE-3Dlite MkIII (with a flat response between 1 Hz to 50 Hz). Data sets were recorded with a 200 Hz frequency rate. A single Cityshark II (18 synchronized channels) 24-bit acquisition system was used to synchronize 6 CMG40-T-1 in March 2019 during the instrumentation of the bell tower. Two Cityshark II were used during the instrumentation of the nave in June 2019 : one to synchronize 6 CMG40-T-1 and another to synchronize 6 LE3Dlite MkIII. 11 setups were performed. The recordings were synchronized using UTC from GPS devices. Each recording lasted one hour according to the empirical rule given by Rodrigues et al. (Rodrigues et al. 2005), where the measurement duration is recommended to be at least 2000 times the natural period of interest. Natural frequencies ( $f$ ) and mode shapes ( $\Phi$ ) of 10 modes have been extracted by using the Enhanced Frequency Domain Decomposition technique (Brincker et al. 2001). Table 1 summarizes the natural frequencies, and Fig. 3 shows the associated mode shapes of the two OMA surveys.

Montabert et al. (Montabert et al. 2022) showed that the building history of the church caused some peculiarities observed in the mode shapes. For example, the first bending mode (mode 1, Fig. 3-a) of the bell tower and the nave shows an out-of-phase mode and reveals a weak connection between these two parts. Historical information and stratigraphic analysis showed that the bell tower was built two centuries after the nave with a still observed joint.

A further example is given by the out-of-phase mode of the facade (mode 4) and one of the two side walls (mode 5) that may have the origin of the described failure mechanism induced by the 1542 earthquake (Montabert et al. 2020).

This high-resolution operational modal analysis is an opportunity to calibrate the church’s initial linear elastic model in its current state by using the extracted natural frequencies and comparing numerical/experimental mode shapes at 81 points. In this study, we use only the first eight modes to update the FE model since mode 9 and mode 10 are at the limit of spatial resolution.

Mode Identifier	Mode description	f (Hz)
1	Bending of the bell tower and nave along the North-South direction in phase opposition	2.61
2	Bending of the bell tower and nave along the West-East direction	2.92
3	Bending of the nave along North-South direction	3.94
4	Bending of the facade	4.96
5	Opening of the nave	5.25
6	Torsional mode of the bell tower	5.82
7	Second bending mode of the bell tower along the North-South direction	6.84
8	Second bending mode of the bell tower along the West-East direction	8.55
9	Third bending mode of the bell tower along the North-South direction	13.95
10	Third bending mode of the bell tower along the West-East direction	18.76

TABLE 1 – Natural frequencies of the Sant’Agata del Mugello church identified (EFDD) in March 2019 and June 2019 (Montabert et al. (2022)).

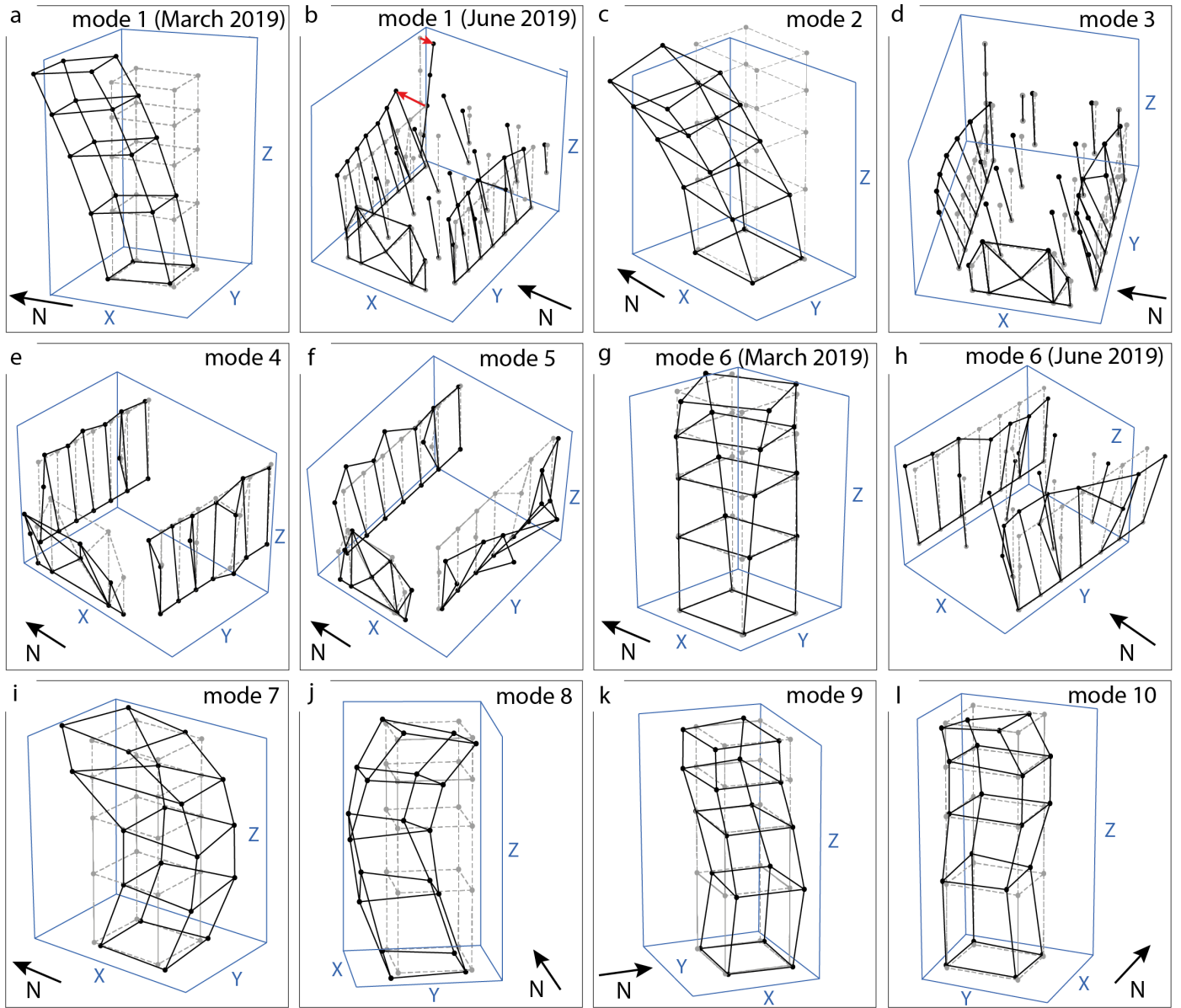


FIGURE 3 – Extracted mode shapes of the church by using the EFDD technique (Montabert et al. (2022)). Dashed grey lines highlight the undeformed mesh. Black lines are related to the extracted mode shape. The black arrow indicates the North building reference. Mode 1-1, mode 2, mode 6-1, mode 7, mode 8, mode 9, and mode 10 were measured in the first survey (in March 2019). Mode 1-2, mode 3, mode 4, mode 5 and mode 6-2 have been extracted from the second survey (in June 2019)

## 4 Updating strategy

The workflow of the model updating process is depicted in Fig. 4. The definition of 5 forward models (step 1, modeling strategies), the sensitivity analysis of model parameters (step 2), and the calibration process (step 3) are detailed hereafter.



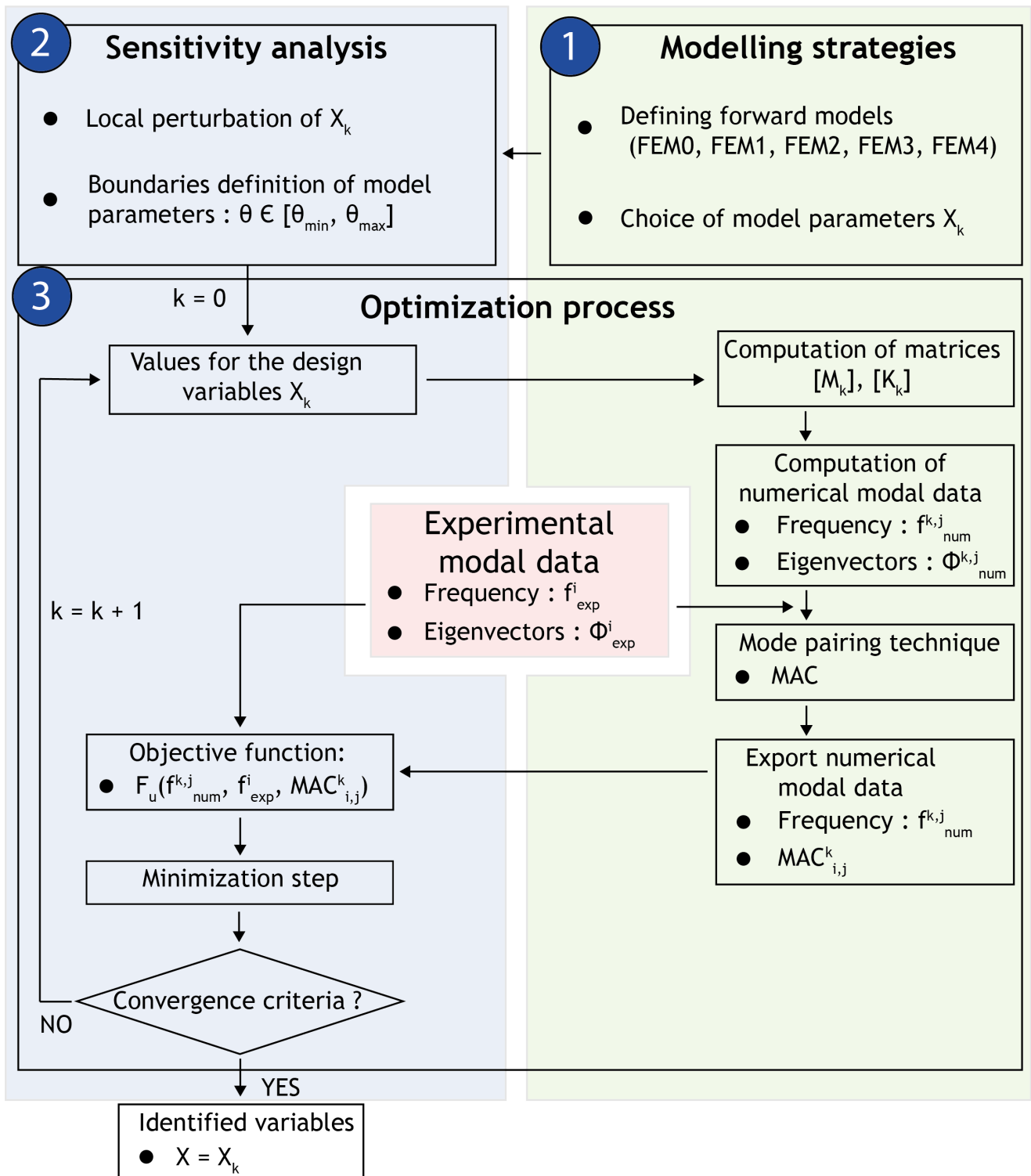


FIGURE 4 – Flow chart of the Vibration-based model updating methodology to calibrate the FE model of the church of Sant'Agata del Mugello.

#### 4.0.1 Modeling strategy

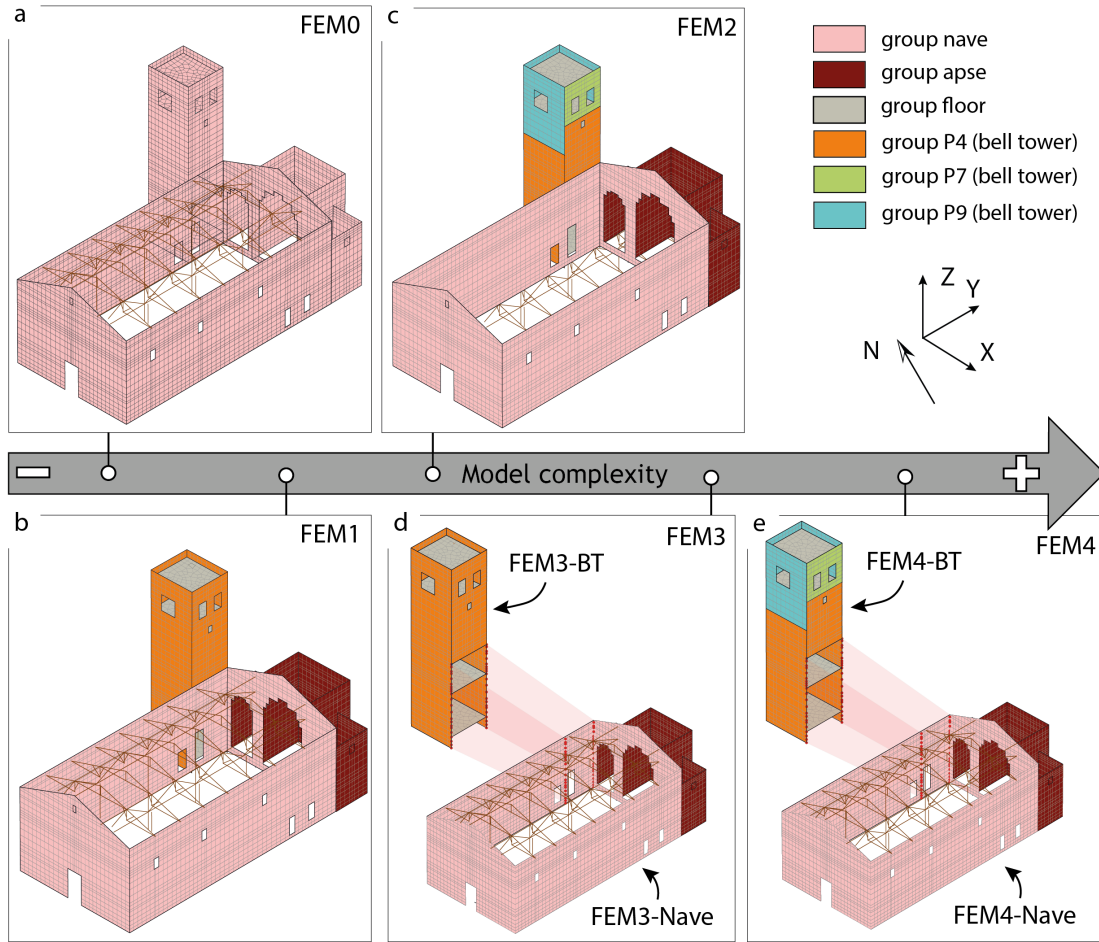


FIGURE 5 – FE modelling strategies FEM0, FEM1, FEM2, FEM3, FEM4.

Five FE models are developed (step 1 in Fig. 4). They are arranged in order of increasing complexity regarding the construction history information used when choosing model parameters. 3D FE models are built using a combination of AutoCAD and the Cast3M software developed by (CEA CEA) assembled in an *ad hoc* python code. The mesh design is based on a TLS point cloud. A relatively large number of finite elements are used to obtain the regular distribution of masses. The load-bearing walls' geometric variations and openings can be reasonably represented. Each model consists of 10049 shell elements (with a size around  $10 \times 10 \text{ cm}^2$ ) with 60630 active degrees of freedom. Secondary elements like bells are not explicitly modeled; their influence was accounted for as added masses.

Since the geometry of the church was accurately surveyed and described in the model, the main uncertainties are related to material properties (Young modulus  $E$ , density  $\rho$ , Poisson coefficient  $\nu$ ) and boundary conditions (the lateral connection between the bell tower, the nave, the apse-chapels block, and the interaction with the ground).

The five forward models with an increasing highlight of the construction history knowledge of Sant'Agata are now described. This knowledge is expressed in terms of material properties whose geometry is inspired by the building phases described in the second section and boundary conditions expressed by lateral stiffness  $K$ . The five forward models range from the most simple to the model, including the highest degree of information from construction history analysis.

**A homogeneous model FEM0** : This basic model is described just by three model parameters : the density  $\rho$ , Young's modulus  $E$ , and the Poisson's ratio  $\nu$  (Fig. 4.0.1-a).

**A block-based model FEM1** : Following the work of Limoge et al. (Limoge 2016), this block-based model (Fig. 4.0.1-b) discretizes the building into three homogeneous blocks in order to enhance the updating process. The

FEM1 contains 9 parameters, 3 per block :  $\{\rho_{BT}, E_{BT}, \nu_{BT}\}$  for the bell tower,  $\{\rho_{Nave}, E_{Nave}, \nu_{Nave}\}$  for the nave, and  $\{\rho_{Apse}, E_{Apse}, \nu_{Apse}\}$  for the apse-chapel part. Note that the nodes at the interfaces of the three blocks are merged.

**A stratigraphic model FEM2** : This model integrates information on construction techniques issued from the stratigraphic analysis (Fig. 4.0.1-c). The construction techniques are classified into 5 groups (Fig. 2). The group nave is described by three model parameters  $\{\rho_{Nave}, E_{Nave}, \nu_{Nave}\}$ . The group apse is characterized by three model parameters  $\{\rho_{Apse}, E_{Apse}, \nu_{Apse}\}$ . Three distinct groups trace the complex history of the bell tower : the initial construction technique "group *tower-P4*"  $\{\rho_{BT-tower-P4}, E_{BT-tower-P4}, \nu_{BT-tower-P4}\}$ ; "group *tower-P7*" is used for reconstructing the southern wall of the church  $\{\rho_{BT-tower-P7}, E_{BT-tower-P7}, \nu_{BT-tower-P7}\}$ ; and the last construction technique "group *tower-P9*" related to the last reconstruction of the bell tower after the 1611 earthquake  $\{\rho_{BT-tower-P9}, E_{BT-tower-P9}, \nu_{BT-tower-P9}\}$ . FEM2 is thus described with 18 model parameters.

**A partitioned model FEM3 (FEM3-BT, FEM3-Nave and FEM3-Apse)** . This model considers the asynchronous construction of the bell tower (Fig. 4.0.1-d). The first built element is the nave, then the bell tower was erected, and finally, the apse.

These asynchronous constructions raise questions about the connection between these three parts of the church. The church is first split into three blocks to be optimized separately : the bell tower block (model FEM3-BT), the nave block (model FEM3-Nave), and the apse block (FEM3-Apse). The model parameters are  $\{\rho_{BT}, E_{BT}, \nu_{BT}\}$  (for material properties),  $\{K_{bx}, K_{by}\}$  (for lateral connection between the bell tower and the nave). FEM3-Nave is initially described by  $\{\rho_{Nave}, E_{Nave}, \nu_{Nave}\}$  for material properties, and  $\{K_{bx}, K_{by}, K_{ax}, K_{ay}\}$  for the lateral connection. FEM3-Apse is described in the same way by  $\{\rho_{Apse}, E_{Apse}, \nu_{Apse}, K_{ax}, \text{ and } K_{ay}\}$ . The impact of soil-structure interaction is also tested with the FE model of the bell tower FEM3-BT through 6 stiffness parameters  $\{K_{ux}, K_{uy}, K_{uz}, K_{mx}, K_{my}, K_{mz}\}$ . The FEM3 model is then described with 23 parameters.

**A stratigraphic partitioned model FEM4 (FEM4-BT, FEM3-Nave, and FEM3-Apse)** : This model is obtained by integrating three construction techniques of the bell tower. The apse and the nave are modeled using FEM3-Apse and FEM3-Nave (no change). The model of the bell tower FEM4-BT is described by the model parameters  $\{\rho_{BT-tower-P4}, E_{BT-tower-P4}, \nu_{BT-tower-P4}, \rho_{BT-tower-P7}, E_{BT-tower-P7}, \nu_{BT-tower-P7}, \rho_{BT-tower-P9}, E_{BT-tower-P9}, \nu_{BT-tower-P9}, K_{bx}, K_{by}\}$ .

Twenty-nine model parameters describe the FEM4 model.

The building techniques of group 9 and group apse comprise heterogeneous size blocks and a substantial quantity of mortar. Groups P4 and P7 use the *a sacco* technique (masonry with a thick inner wall and a thinner outer wall, where the gap was filled with stones and mortar). Even in this context, recent studies adopting a homogeneous and isotropic material for masonry have successfully investigated the dynamic and seismic response of different typologies of historical masonry constructions (e.g., [Milani et al. 2017](#) ; [Valente 2021](#)). Materials are then modeled as homogeneous and isotropic in all strategies.

A two steps optimization process is performed for FEM3 and FEM4. The first process consists in updating each substructure separately : FEM3-BT, FEM3-Apse, FEM3-Nave for the FEM3 modeling strategy, and FEM4-BT, FEM3-Apse, FEM3-Nave for the FEM4 modeling strategy. Interaction between each substructure is taken into account through stiffness ( $K_x, K_y$ ) between the nodes of the substructure and fixed nodes. They can be seen as apparent stiffnesses. The second step is focused on the updating of  $K_x, K_y$  (varying in a wide range unlike the material parameters optimized in step 1) between nodes of the two substructures (tower and nave).  $K_x$  and  $K_y$  correspond to the actual linear stiffness, which are finally retained.

## 4.1 Sensitivity Analysis and value bounds

The FEM0, FEM1, FEM2, FEM3, and FEM4 modeling strategies require the solution of 3, 9, 18, 23, and 29 model parameters, respectively. As our objective function includes only eight modes, determining the model parameters of FEM1, FEM2, FEM3, and FEM4 is an underdetermined problem implying the non-unicity of the solution problem. The first step is to assess the relevance of each model parameter through a sensitivity analysis. A local perturbation of the model parameters (step 2 in Fig. 4). As proposed by [Gentile et al. 2015](#), we compute the sensitivity coefficient ( $s_{i,k} = \partial f_i^{num} / \partial X_k$ ) as the rate of change of the natural frequencies concerning a change in a model parameter as defined in its normalized form :

$$s_{i,k} = 100 \frac{X_k}{f_i^{num}} \frac{\partial f_i^{num}}{\partial X_k} \quad (1)$$

where  $f_i^{num}$  ( $i \in [1, M]$ ) is the  $i$ -th natural frequency of the model and  $X_k$  ( $k \in [1, N]$ ) is the  $k$ -th parameter to be identified. The sensitivity analysis is performed by considering only natural frequencies since they are mainly impacted by the selected model parameters (mostly related to material properties).

The sensitivity coefficients as a function of mode frequency are shown in Fig. 6-7 for the parameters describing FEM0, FEM1, FEM2, FEM3-BT, and FEM4-BT. The tested input parameters are shown on the X-axis. The Y-axis corresponds to the mode frequencies computed by each forward model. Dark blue highlights high values of sensitivity coefficients. It was chosen to keep only the mechanical parameters with a sensitivity coefficient  $> 5\%$ . Lower and upper bounds are described for each parameter. Initial values used for the sensitivity analysis are  $E = 1 \text{ GPa}$ ,  $\rho = 12 \text{ kN/m}^3$  and  $\nu = 0.2$ .

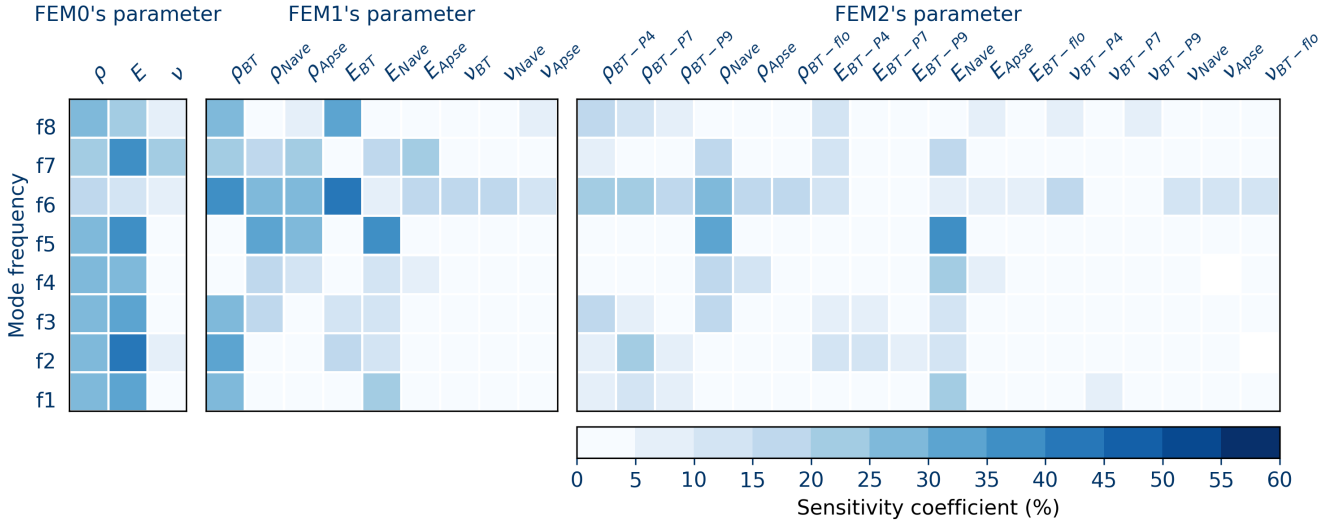


FIGURE 6 – Sensitivity coefficients for FEM0 (left), FEM1 (middle) and FEM2 (right).  $\rho$  is the mass density,  $E$  the Elastic Young’s modulus,  $\nu$  the Poisson’s ratio, while the subscript BT indicates bell tower.

In the case of the FEM0 model (Fig. 6, on the left), we find that all eight frequencies have a sensitivity greater than 10% to the density ( $\rho$ ) and Young’s modulus ( $E$ ). The Poisson’s ratio ( $\nu$ ) impacts the frequency of modes 2, 6, and 7. The three material parameters are therefore used in the optimization process.

For the FEM1 model (Fig. 6, on the middle), the eight frequencies are sensitive to the densities  $\{\rho_{BT}, \rho_{Nave}, \rho_{Apse}\}$ . Only the frequency of the torsion mode (f6) has a sensitivity  $> 10\%$  for the Poisson coefficients of the three parts  $\{\nu_{BT}, \nu_{Nave}, \nu_{Apse}\}$ . The nine parameters are used.

For the FEM2 model, the bell tower’s densities  $\{\rho_{BT-tower-P4}, \rho_{BT-tower-P7}, \rho_{BT-tower-P9}\}$ , and the Young’s moduli  $\{E_{BT-tower-P4}, E_{BT-tower-P7}, E_{BT-tower-P9}\}$  have a sensitivity coefficient  $> 5\%$  on bell tower’s frequencies. However, they have little impact on the frequencies f4 and f5 associated with the nave’s frequencies. The material parameters of the floor  $\{\rho_{floor}, E_{floor}, \nu_{BT-tower-P4}\}$  are also retained in the optimization since they have an impact on f6 (torsion mode) up to 20%. The Poisson’s ratio  $\{\nu_{BT-tower-P4}, \nu_{floor}, \nu_{nave}, \nu_{apse}\}$  induce a sensitivity coefficient  $> 10\%$  on the f6 frequency and  $\{\nu_{BT-tower-P7}, \nu_{BT-tower-P9}\}$  induce a sensitivity coefficient  $> 5\%$  on the f1 mode. All 18 parameters are kept.

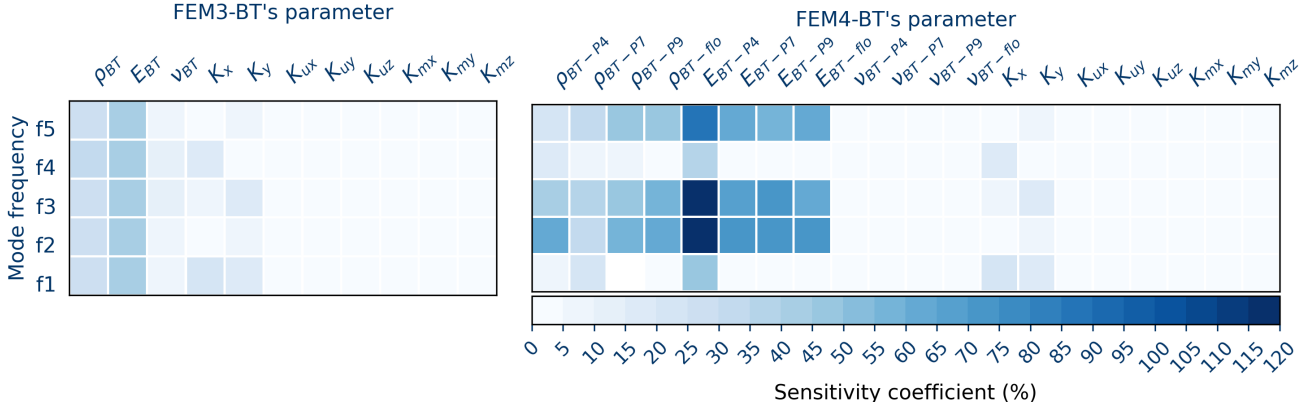


FIGURE 7 – Sensitivity coefficient for FEM3 and FEM4

For the FEM3 modeling strategy, a sensitivity analysis is conducted on the FEM3-BT model. The variations of the density  $\rho_{BT}$ , of Young’s modulus  $E_{BT}$  and of the lateral stiffnesses between the bell tower and the nave  $\{K_{bx}, K_{by}\}$  have a sensitivity coefficient  $> 5\%$  (Fig. 7) and are thus retained in the optimization process. The modeling of the interface stiffness between the bell tower and the ground  $\{K_{ux}, K_{uy}, K_{uz}, K_{mx}, K_{my}, K_{mz}\}$  induce a sensitivity coefficient lower than 0.1%. Furthermore, they have a small impact on the mode shapes and are not retained for optimization. For the model of the nave FEM3-NAVE and the apse-chapel part, the densities, Young’s moduli, and Poisson’s coefficients are retained since the sensitivity is higher than 5%. In the same way,  $\{\rho_{Nave}, E_{Nave}, \nu_{Nave}, \rho_{Apse}, E_{Apse}, \nu_{Apse}\}$  show a sensitivity coefficient over 5%. On the contrary, the lateral stiffness  $\{K_{ax}, K_{ay}\}$  between the nave and the apse did not affect either the frequencies ( $s_{i,k} < 1\%$ ) or the mode shapes, so they are excluded from the optimization process. The number of model parameters of FEM3 is reduced to 11 instead of 23.

Fig. 7 shows how sensitive is the model of the bell tower FEM4-BT to the density and Young’s moduli of each building phase. Only the Poisson’s ratios  $\{\nu_{BT-tower-P4}, \nu_{BT-tower-P7}, \nu_{BT-tower-P9}\}$  and the two lateral stiffness  $\{K_{bx}, K_{by}\}$  are not retained since they have a sensitivity coefficient  $s_{i,k} < 1\%$ .

Regarding the lower-higher bounds for each parameter in the searching procedure, several studies use the values provided by the Italian Technical Standards for Structure (NTPC 2018) or regional databases based on analogous materials to constrain the limits of the range of variation of mechanical parameters. Aware of the variability of the parameter values, especially in the case of a historical building, we propose, on the contrary, to explore a wide range of values for all strategies taking advantage of the performance of the multiprocessing PSO code. Similar lower and upper bounds of the elastic parameters of FEM0, FEM1, FEM2, FEM3 and FEM4 are taken and shown in Table 2.

Updated parameter	$\rho$ [ $kN.m^{-3}$ ]	$E$ [MPa]	$\nu$ [-]	K [N.m]
Min.	15	100	0.05	1
Max.	35	10000	0.4	1e10

TABLE 2 – Lower and upper bounds for elastic properties for FEM0, FEM1, FEM2, FEM3 and FEM4 ( $\rho$  is the mass density, E the Elastic Young’s modulus,  $\nu$  the Poisson’s ratio).

## 4.2 Particle Swarm Optimization Algorithm

The optimization process is performed through a Particle Swarm Optimisation (PSO) algorithm. The algorithm is introduced by Eberchart and Kennedy 1995. It is a bio-inspired population-based stochastic technique called an evolutionary computational model based on swarm intelligence. Each particle is randomly clustered through the search space. The particle records and communicates with other particles about the best solution (best local position) they find. PSO has been used in many studies (e.g. Shabbir and Omenzetter 2014, Kayashima et al. 2017, Tran-Ngoc et al. 2018) and many disciplines (physics, structural mechanics, geosciences, etc.) to solve ill-conditioned optimizations problems. The PSO is based on two equations. The first equation (Eq. 2) updates the position of a particle. The second equation (Eq. 3) updates its velocity.

$$x_i^{t+1} = x_i + v_i^{t+1} \quad (2)$$

$$v_i^{t+1} = \omega v_i^t + c_1 r_1 (p_i^t - x_i^t) + c_2 r_2 (p_{gbest} - x_i^t), \quad (3)$$

where  $x_i^t$ , and  $x_i^{t+1}$  represent the position vectors of particle  $i$  at time  $t$ ,  $\omega$  is the inertia weight parameter,  $c_1$  and  $c_2$  are the cognition learning factor and the social learning factor,  $r_1, r_2$  are random between 0 and 1,  $p_i^t$  is the local best position of each particle, and  $p_{gbest}$  is the global best position of all particles. Each particle is characterized by a velocity vector and a position vector in space. In the updating process, particles can remember the best local position  $p_i^t$  and communicate with others to look for the global best position  $p_{gbest}$ . PSO develops iterations to determine the state of each particle based on the objective function. The global best position ( $p_{gbest}$ ) is achieved when the objective function is minimum. Because only a few parameters need to be tuned, PSO tends to converge to the global best position faster than other optimization algorithms, resulting in faster computation time and a better correlation between observable and predicted parameters.

After performing manual sensitivity tests, the PSO parameters are taken such that  $\omega = 0.5$ ,  $c_1 = 0.5$ , and  $c_2 = 0.5$  in agreement with those proposed by Wang et al. 2018. Nevertheless, the number of particles ( $S$  in the following) is deeply related to the number of model parameters. As discussed later, several optimization processes are run with an increasing number of particles.

The model updating process using the PSO algorithm was set to stop when the residual tolerance of two consecutive steps reached 1e-4 or after 1000 evaluations (the results shown below have never reached this last criterion), ensuring the stability of the iterative solution.

Because we are dealing with stochastic algorithms, the optimization process is carried out many times with a different search space to ensure that the global minima of the function have been found (Ceravolo et al. 2016).

### 4.3 Optimization process

**Modal analysis** The starting point of the VBMU (step 3 in Fig. 4) is the initialization of the parameters to be updated  $X_k$  at step  $k$ . The mass matrix  $[M_k]$  and stiffness matrix  $[K_k]$  are then computed in Cast3M after integrating constraints introduced by the different modeling strategies (FEM0, FEM1, FEM2, FEM3, FEM4). Numerical eigenfrequencies  $f_{num}^{k,j}$  and mode shapes  $\{\Phi_{num}^{k,j}\}$  of the building are then computed through modal analysis.

**Mode pairing technique** The mode pairing technique consists of identifying the pairs of experimental/numerical modes by selecting the maximum Modal Assurance Criterion (MAC) value between the experimental and the numerical modes shapes ( $\phi_{exp}$  and  $\phi_{num}$ ) expressed as :

$$MAC = \frac{|\{\phi_{num}\}^H \{\phi_{exp}\}|^2}{|\{\phi_{num}\}^H \{\phi_{num}\}| |\{\phi_{exp}\}^H \{\phi_{exp}\}|} \quad (4)$$

This mode pairing operation ensures that the numerical modal basis is organized as measured. This is a crucial criterion for consistency with the measures.

**Objective function** An objective function quantifies the difference between the numerical and experimental dynamic parameters. Its definition impacts the optimization results. A list of the frequently used objective functions in the literature and tested for Sant'Agata is presented in Table 3. The four functions are then tested since their efficiency evolves as a function of the forward model.

Name	Definition	References
$F_1$	$\sum_{i=1}^n \frac{\max MAC_{i,j}}{n}$	e.g., Limoge (2016), Azzara et al. (2019), Gunaydin et al. (2018)
$F_2$	$\sum_{i=1}^n \sqrt{\frac{(f_{exp}^i - f_{num}^j)^2}{(f_{exp}^i)^2}}$	e.g., Limoge (2016), Ribeiro et al. (2012), Gunaydin et al. (2018)
$F_3$	$\alpha.F_1 + \beta.F_2$	e.g., Limoge (2016)
$F_4$	$1 - \alpha.F_1 * [1 - \beta.F_2]$	e.g., Limoge (2016)

TABLE 3 – Objective functions used in the optimization process.  $\alpha$  and  $\beta$  are weighting factor assigned to function.  $\alpha = \beta = 0.5$  in this study.

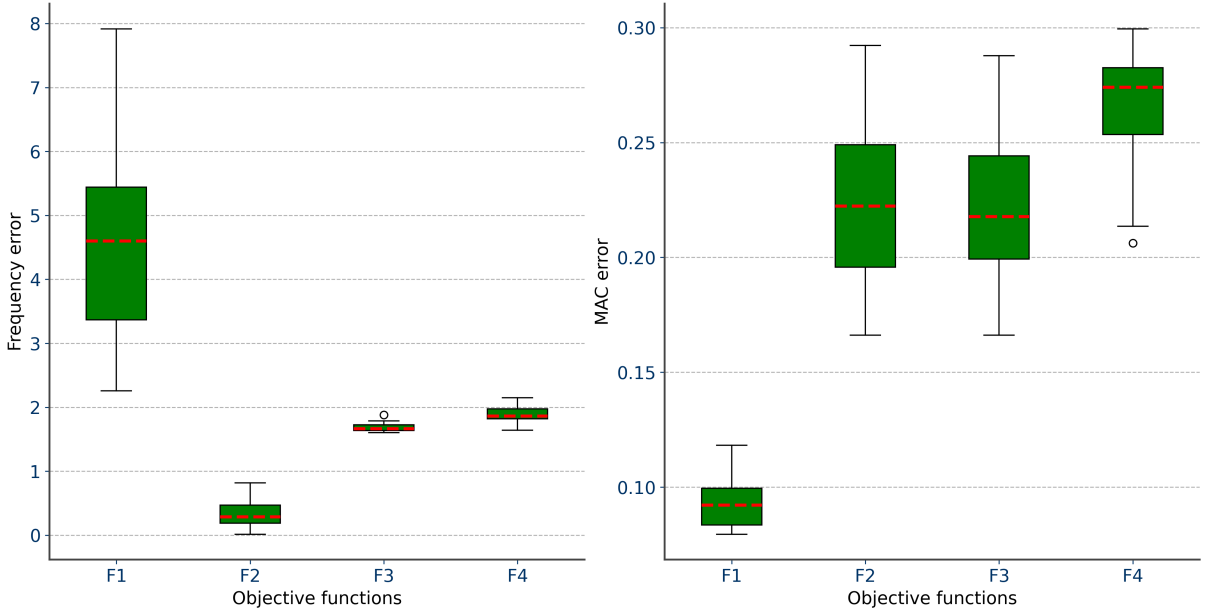


FIGURE 8 – Frequency errors and MAC error obtained for model FEM3-BT according to the different objective functions used (F1, F2, F3 and F4).

The  $F_1$  function (Table 3) optimizes by using the MAC criterion. It is thus only based on comparing the numerical mode shapes with the experimental ones. Let us suppose that the function is relevant for calibrating the boundary conditions controlling the quality of the mode shape. In that case, it may fail to reorganize the modes since it does not impact the natural frequencies.

On the contrary, the  $F_2$  function (Table 3) is focused on the frequencies. F2 allows refining the model parameters related to material properties but has no control over the boundary conditions. Functions  $F_1$  and  $F_2$  are massively used for VBMU of conventional Reinforced Concrete buildings. Gunaydin et al. (2018) shows how easy it is to optimize an RC building using one of the two functions separately. The authors quickly get a very high MAC value (0.99 for each of the four measured modes) by direct use of the manual tuning technique. However, this process is not so easily applicable to an ancient masonry building that induces complex mode shapes with local behavior (e.g., Limoge 2016).

The function  $F_3$  (Table 3) seems a suitable compromise in our case since it combines functions  $F_1$  and  $F_2$ . A weighting factor is assigned according to whether one gives more importance to the mode shape comparison ( $\alpha$ ) or to the frequency ( $\beta$ ). However, depending on the weighting factor that is assigned to the mode shape and the frequency, the function  $F_3$  sometimes cannot find the appropriate pairing mode because it is too far away in frequency.

This problem may be solved by the function  $F_4$  (Table 3), which weights the mode shape's comparison by the frequency discrepancy. A different weighting factor can still be assigned depending on whether the natural frequency is given more importance than the mode shape.

The performance of the objective functions summarized in Tab. 3 are tested with two different typologies : the bell tower (FEM3-BT) and the nave (FEM3-Nave); 20 runs of the optimization process are performed with FEM3-BT and FEM3-Nave by using each objective function (F1, F2, F3, F4).

The final errors of each run are expressed in terms of frequency error ( $\sum_{i=1}^n \sqrt{\frac{(f_{exp}^i - f_{num}^j)^2}{(f_{exp}^i)^2}}$ ) and MAC error ( $\sum_{i=1}^n \frac{\max MAC_{i,j}}{n}$ ) as reported in Fig. 8 and 9. The characteristics of the PSO algorithms are a population of 500 particles,  $c_1 = 0.5$ ,  $c_2 = 0.5$ , and  $\omega = 0.5$ . F3 and F4 functions are expressed using  $\alpha = \beta = 0.5$ . These results are consistent with similar tests by Limoge 2016.

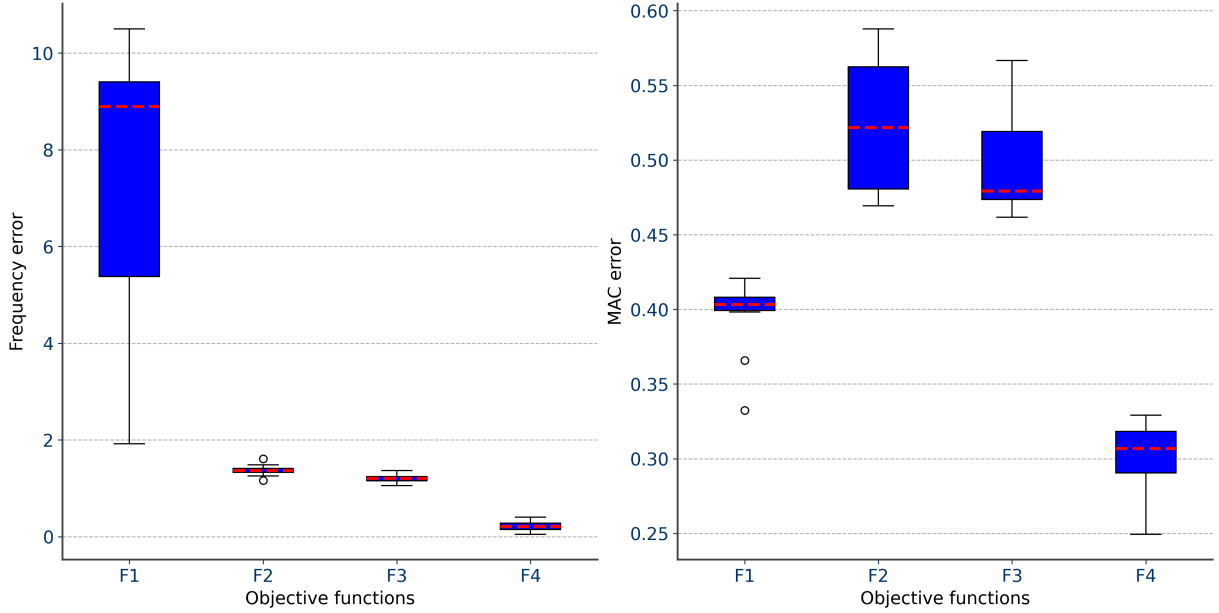


FIGURE 9 – Frequency errors and MAC error obtained for model FEM3-Nave according to the different objective functions used (F1, F2, F3 and F4).

Five modes are used for the optimization of FEM3-BT, namely 1, 2, 6, 7 and 8 in Table 3, and five modes for the FEM3-Nave, namely 1, 3, 4, 5, and 6 in Table 3).

In the case of FEM3-BT, the F1 objective function leads to the best mode shape optimization (Fig. 8, right) but induces a wide distribution of higher modal frequency errors (Fig. 8, left). The F2 objective function highlights the lowest frequency errors and is equivalent to F3 and F4 for mode shape optimization.

The nave is a broader structure with more complex modes than a slender structure. Fig. 9 shows that objective functions F2 and F3 based on frequency minimization induce a significant error in mode shape results. F1 leads to a significant error in frequency optimization. The lowest error in frequency and mode shapes is obtained with the F4 objective function (Fig. 9).

F2 is the most suitable objective function for optimizing the bell tower. F4 is more appropriate for the nave. The F2 function is then used to update the design variables of FEM3-BT and FEM4-BT. F4 is then used for optimizing FEM0, FEM1, FEM2 and FEM3-Nave (with  $\alpha = 0.5$  and  $\beta = 0.5$ ).

## 5 Results of the updating process

The five models (FEM0, FEM1, FEM2, FEM3, and FEM4) are updated using the aforementioned process. In order to assess stability and limit local minima, the PSO algorithm is run many times. Initial values of model parameters are randomly distributed for each run. PSO was run 20 times for FEM0, FEM1, FEM2, and FEM3-Nave and 50 times for FEM3-BT and FEM4-BT for 10, 50, 100, 200, 500, and 1000 particles. The mean and standard deviation values of each process’s objective function (F2 and F4) are shown in Fig. 10.



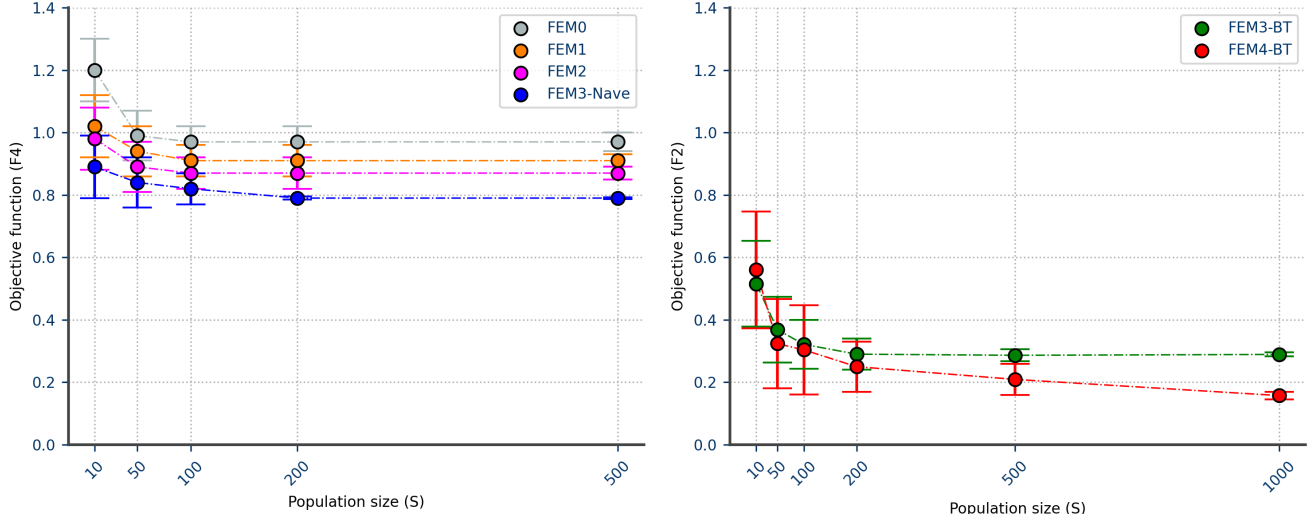


FIGURE 10 – Left - Evolution of the objective function F4 for models FEM0, FEM1, FEM2 and FEM3-Nave. For each value of S, filled circles with bars are mean values of F4 after 20 simulations with standard error. Right - same as left for objective function F2, models FEM3-BT and FEM4-BT and 50 simulations for each value of S.

Exp. mode		FEM0				FEM1				FEM2			
#	$f_{exp}$ [Hz]	#	$f_{num}$ [Hz]	$\Delta f$ [%]	MAC	#	$f_{num}$ [Hz]	$\Delta f$ [%]	MAC	#	$f_{num}$ [Hz]	$\Delta f$ [%]	MAC
1	2.61	1	2.48	4.98	0.98	1	2.41	7.66	0.97	1	2.48	4.98	0.98
2	2.92	8	2.82	3.42	0.91	2	2.80	4.11	0.83	2	2.72	6.85	0.70
3	3.94	1	2.48	37.06	0.94	9	3.58	9.14	0.95	8	3.30	16.24	0.84
4	4.96	10	5.51	11.09	0.93	10	4.11	17.14	0.88	10	4.91	1.01	0.73
5	5.25	13	6.20	18.10	0.71	14	5.88	12.0	0.51	12	5.14	2.10	0.55
6	5.82	12	6.00	3.09	0.78	14	5.88	1.03	0.77	18	5.80	0.34	0.78
7	6.84	16	7.31	6.87	0.78	24	7.08	3.51	0.52	23	7.15	4.53	0.55
8	8.55	20	8.48	0.82	0.90	28	8.19	4.21	0.92	28	8.64	1.05	0.52

TABLE 4 – Modal parameters of the best updated model for FEM0, FEM1 and FEM2 after calibration. Results are compared to experimental modes in terms of frequency ( $\Delta f = \|f_{num} - f_{exp}\|/f_{exp}$ ), mode ranking (#), and MAC.

## 5.1 Models FEM0, FEM1 and FEM2

FEM0, FEM1, and FEM2 models reach a minimum value of objective function F4 from a population size of 100 particles. The best models' dynamic parameters are expressed in terms of numerical frequencies and MAC in Table 4.

Optimizing the FEM0 model faces two difficulties (Table 4). Numerical mode 1 is identified twice (numerical mode 1 is identified as the best correspondent of experimental modes 1 and 3), and modes 12 and 13 are inverted, although experimental modes 5 and 6 are successfully identified. In the first case, the mode pairing operation fails to discriminate the pairs. For  $\phi_{exp}^3$ , the best MAC criterion of 0.94 (Table 4) is obtained for the pair  $\{\phi_{exp}^3, \phi_{num}^1\}$  while the correct pair  $\{\phi_{exp}^3, \phi_{num}^9\}$  only get the second-best MAC of 0.92 (not shown here since Table 4 shows the best pair which is  $\{\phi_{exp}^3, \phi_{num}^1\}$ ) which cannot then be retained.

Fig. 11 shows the scalar product between pairs  $\{\phi_{exp}^1, \phi_{num}^1\}$  (on the left) and  $\{\phi_{exp}^3, \phi_{num}^9\}$  (on the right) at the node-scale (known as the Coordinate Modal Assurance Criteria).

This finer analysis, shown in Fig. 11, reveals nodes with lower correlation coefficients at the nodes W1, W2, and W3 (see Fig. 11) and the interface between the nave and the bell tower. AVTs were performed at W1, W2, and W3 under strong winds (windows were opened). Furthermore, the temperature along the windows was higher than in any other location in the church (survey during a hot June). We propose to attribute the unexpected modal

displacement mainly to environmental conditions.

The noise records at nodes close to the interface between the nave and the bell tower are also poorly correlated (see Fig. 11). These nodes were recorded in the same condition as all others nodes (inside the church). Therefore, the unexpected modal displacement is unlikely related to the dynamic identification tests. On the contrary, this is probably related to a singularity of the structure that has not been taken into account in the modeling. In particular, this leads to disturbing the mode pairing step. Indeed, the pair  $\{\phi_{exp}^3, \phi_{num}^9\}$  is correctly identified when removing these nodes in the optimization process (numerical modes related to  $\phi_{exp}^5$  and  $\phi_{exp}^6$  are however still inverted inducing a fundamental error in the objective function).

We propose to explain this behavior at the interface between the nave and the bell tower by the late construction of the former along the latter (2 centuries after the nave). A large joint between the two parts of the building is clearly visible. This observation will be used to optimize rigidity values at the interface between the bell tower and the nave (FEM3 and FEM4 models). However, we are aware of the limitations of this new modeling strategy beyond the linear hypothesis since the weak nave/tower connection is likely associated with non-linear stiffness.

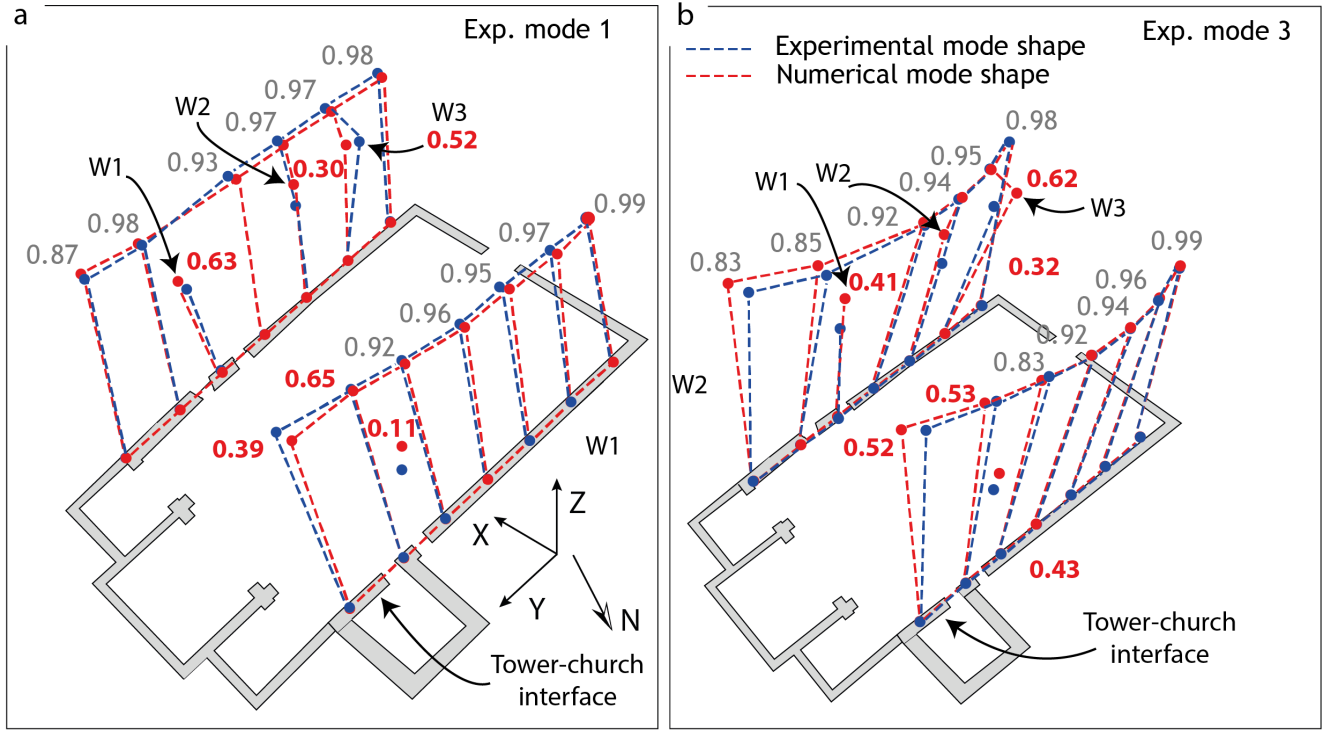


FIGURE 11 – Scalar product between numerical mode shape in red of FEM0  $\phi_{num}^1$  and experimental mode shape  $\phi_{exp}^1$  in blue (a) and the modes pair  $\{\phi_{exp}^3, \phi_{num}^9\}$  (b).

The optimization of model FEM1 leads to a smaller value of F4 (Fig. 10 on the left). This is partially explained by the identification of the pair  $\{\phi_{exp}^3, \phi_{num}^9\}$  with yet a MAC of 0.83 (Table 4). Furthermore, this model does not allow to distinguish  $\{\phi_{exp}^5, \phi_{num}^{14}\}$  and  $\{\phi_{exp}^6, \phi_{num}^{14}\}$  leading to a large frequency error ( $\Delta f$  equal to 12.0 % for mode pair  $\{\phi_{exp}^5, \phi_{num}^{14}\}$  in Table 4).

With the FEM2 model, based on the stratigraphic reading of the church wall, a more significant reduction of F4 is reached. In particular, the modal base is now properly ordered (Table 4, columns FEM2). However, the numerical modes 2 and 3 have a frequency error  $\Delta f$  still over 5 %.

The values of the best model parameters are shown in Table 5 along with the standard deviation ( $\sigma$ ) of the model parameters of the best models from the 20 optimization processes. The standard deviation values highlight a wide distribution of the solutions, which unfortunately demonstrates the inability of the FEM2 model to converge towards a unique solution.

Density [ $kN.m^{-3}$ ]			Young's Modulus [ $MPa$ ]			Poisson's ratio [-]		
Parameter	Best sol.	$\sigma$	Parameter	Best sol.	$\sigma$	Parameter	Best sol.	$\sigma$
$\rho_{BT-P4}$	17.00	4.09	$E_{BT-P4}$	504	137	$\nu_{BT-P4}$	0.10	0.11
$\rho_{BT-P7}$	15.05	4.99	$E_{BT-P7}$	1540	994	$\nu_{BT-P7}$	0.19	0.09
$\rho_{BT-P9}$	16.42	3.44	$E_{BT-P9}$	3770	1080	$\nu_{BT-P9}$	0.13	0.11
$\rho_{BT-flo}$	24.49	5.45	$E_{BT-flo}$	675	1520	$\nu_{BT-flo}$	0.37	0.09
$\rho_{Nave}$	31.73	1.44	$E_{Nave}$	3010	1020	$\nu_{BT-Nave}$	0.12	0.10
$\rho_{Apse}$	27.22	6.28	$E_{Apse}$	1210	958	$\nu_{BT-Apse}$	0.26	0.09

TABLE 5 – Updated parameter of the model FEM2 expressed in terms of best solution (obtained from the minimal objective function F4) and standard deviation ( $\sigma$ ) of all solutions (for  $S = 200$  particles).  $\rho$  is the mass density, E the Elastic Young's modulus,  $\nu$  the Poisson's ratio, while the subscripts BT indicates bell tower, *flo* indicates floor of the bell tower, P4, P7, P9 indicate the technique group associated with phase 4, phase 7 and phase 9 respectively.

## 5.2 Adding boundary conditions (model FEM3) and stratigraphic analysis (model FEM4)

Exp. mode		FEM3-BT				FEM4-BT				FEM3-Nave			
#	$f_{exp}$ [Hz]	#	$f_{num}$ [Hz]	$\Delta f$ [%]	MAC	#	$f_{num}$ [Hz]	$\Delta f$ [%]	MAC	#	$f_{num}$ [Hz]	$\Delta f$ [%]	MAC
1	2.61	1	2.37	9.20	0.93	1	2.58	1.15	0.98	1	2.65	1.53	0.92
2	2.92	2	2.51	14.04	0.86	2	2.92	<0.01	0.91	-	-	-	-
3	3.94	-	-	-	-	-	-	-	-	3	3.62	8.12	0.66
4	4.96	-	-	-	-	-	-	-	-	5	4.85	< 0.01	0.75
5	5.25	-	-	-	-	-	-	-	-	6	5.05	3.81	0.52
6	5.82	3	6.08	4.47	0.90	3	5.82	<0.01	0.91	7	5.86	0.69	0.53
7	6.84	4	6.84	<0.01	0.72	4	6.86	0.29	0.85	-	-	-	-
8	8.55	5	8.53	0.23	0.44	5	8.55	<0.01	0.42	-	-	-	-

TABLE 6 – Modal parameters of the best updated model for FEM3-BT, FEM4-BT and FEM3-Nave after calibration. Results are compared to experimental modes in terms of frequency ( $\Delta f = \|f_{num} - f_{exp}\|/f_{exp}$ ), mode ranking (#), and MAC.

The FEM3 strategy aims to optimize the bell tower (FEM3-BT) and the nave (FEM3-Nave) separately. A stiffness  $K_{bx}$  and  $K_{by}$  between the bell tower and the nave is therefore added to the parameters to be optimized. The objective function F2 converges to the lowest value 0.28, from 200 particles. The optimization process is run 50 times for each population size  $S$  of 10, 50, 100, 200, 500, and 1000 particles. The optimization process for the FEM3-BT model converges to the lowest values of F2 0.28, starting at 200 particles (Fig. 10, right). The modal parameters of the best optimization are shown in Table 6.

The frequency error is still too high for the first two modes (modes 1 and 2). Only mode 7 is evaluated with a frequency error lower than 1 %. The updated parameter distribution for the best solutions is illustrated in Fig. 12 where a convergence of the model parameters is observed for three values of  $S$  (100, 500, and 1000). The values of the best model parameters for FEM3-BT are shown in Tables 7 along with the standard deviation ( $\sigma$ ) of the model parameters of the best 50 models from the optimization process.

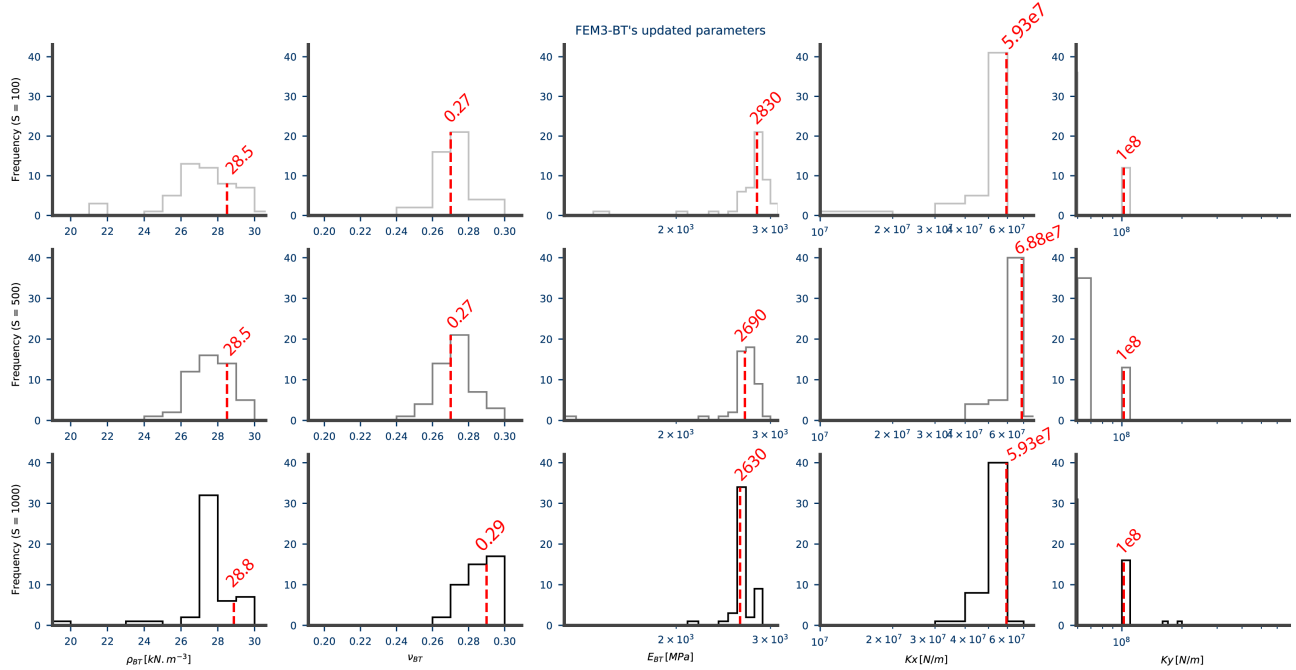


FIGURE 12 – Distribution of the updated design variables for the best 50 runs for the model FEM3-BT for 100 (top), 500 (middle) and 1000 (bottom) particles. Values of updated parameters of the best model in term of objective function are plotted in dashed red.

	$\rho_{BT} [kN.m^{-3}]$	$E_{BT} [MPa]$	$\nu_{BT} [-]$	$K_x [N.m]$	$K_y [N.m]$
<b>Best sol.</b>	28.8	2630	0.29	5.93e7	1.02e8
$\sigma$	1.7	122	0.01	5.98e6	4.58e8

TABLE 7 – Updated parameter of the model FEM3-BT expressed in terms of best solution (obtained from the minimal objective function F2) and standard deviation ( $\sigma$ ) of all solution (for S = 200 particles).  $\rho$  is the mass density, E the Elastic Young’s modulus,  $\nu$  the Poisson’s ratio, while the subscripts BT indicates bell tower.

Density [ $kN.m^{-3}$ ]			Young’s Modulus [ $MPa$ ]			Poisson’s ratio [-]			Lateral Stiffness [ $N.m$ ]		
Parameter	Best sol.	$\sigma$	Parameter	Best sol.	$\sigma$	Parameter	Best sol.	$\sigma$	Parameter	Best sol.	$\sigma$
$\rho_{Nave}$	31.1	6.3	$E_{Nave}$	2260	8.47	$\nu_{Nave}$	0.42	0.11	$K_x$	1.7e8	0.8e8
$\rho_{Apse}$	15.2	1.5	$E_{Apse}$	1040	1.56	$\nu_{Apse}$	0.24	0.09	$K_y$	6.02e9	1.23e8

TABLE 8 – Updated parameters of the model FEM3-Nave expressed in terms of best solution (obtained from the minimal objective function F4) and standard deviation ( $\sigma$ ) of all solution (for S = 200 particles).  $\rho$  is the mass density, E the Elastic Young’s modulus,  $\nu$  the Poisson’s ratio, while the subscripts K indicates the lateral stiffness along the bell tower.

**Model updating of the nave** The optimization process of the FEM3-Nave model results in a minimum of 0.79 for the objective function F4 for 200 particles. The modes are arranged correctly (Table 6). Only the mode associated with experimental mode 3 is obtained with a deviation higher than 5 %. The error in MAC is also important due to the large number of nodes and the associated errors in their measurement. The standard deviation exhibits a small variability of the design variables (density, Young modulus, and lateral stiffness in Table 8).

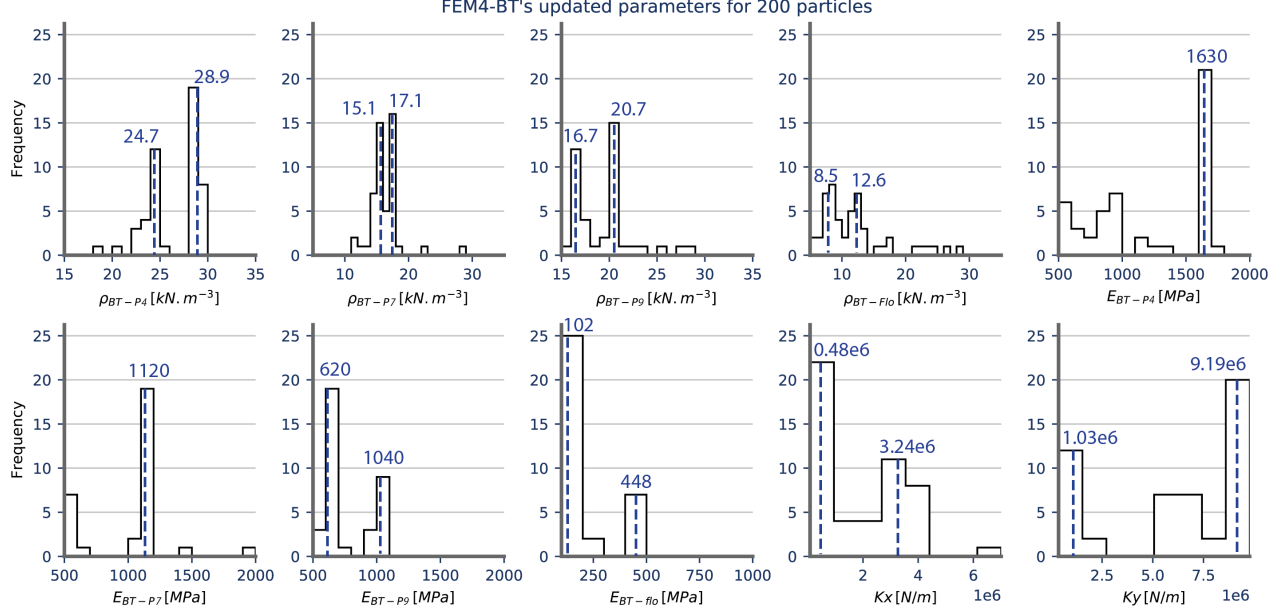


FIGURE 13 – Distribution of the results for the model FEM4-BT.

Density [ $kN.m^{-3}$ ]			Young's Modulus [ $MPa$ ]			Lateral stiffness [ $N.m$ ]		
Parameter	Best sol.	$\sigma$	Parameter	Best sol.	$\sigma$	Parameter	Best sol.	$\sigma$
$\rho_{BT-P4}$	28.9	0.8	$E_{BT-P4}$	1630	463	$K_x$	1.8e6	1.75e5
$\rho_{BT-P7}$	15.1	0.2	$E_{BT-P7}$	1120	623	$K_y$	9.08e6	3.92e5
$\rho_{BT-P9}$	16.7	0.2	$E_{BT-P9}$	620	14			
$\rho_{BT-flo}$	8.05	529	$E_{BT-flo}$	102	9			

TABLE 9 – Updated parameter of the model FEM4-BT expressed in terms of best solution (obtained from the minimal objective function F4) and standard deviation ( $\sigma$ ) of all solution (for  $S = 200$  particles).  $\rho$  is the mass density, E the Elastic Young's modulus, while the subscripts BT indicates bell tower, *flo* indicates floor of the bell tower, P4, P7, P9 indicate the technique group associated with phase 4, phase 7 and phase 9 respectively.

The optimization process of the FEM4-BT model results in a minimum value of 0.15 for the F2 objective function. The objective function's value is lower than that of FEM3-BT when using 200 particles. The higher the number of particles, the lower the standard deviation of F2. FEM4-BT is, however, the forward model using the highest number of model parameters. Fig. ??-13 show the distribution of model parameters of 50 runs for 200, 500, and 1000 particles, respectively. When using 200 particles, most of the modal parameters show two possible solutions compatible with the expected value for masonry (Fig. ??). Unfortunately, the impossibility of carrying out additional even rough characterization of the material does not allow us to conclude about the best solution.

When increasing the number of particles to 500, the distribution of the model parameter is narrower, and a few parameters ( $\rho_{BT-P7}$ ,  $\rho_{BT-flo}$ ,  $E_{BT-P7}$ ,  $BT - flo$ ) converge toward a unique solution. When using 1000 model parameters, model parameters finally converge toward a unique solution except for the lateral rigidity  $K_x$ , and  $K_y$ . By default, we finally choose the values of model parameters obtained for the minimum value of the objective function (shown in red in Fig. 13). The modal characteristics of this best model are presented in Table 6 (column FEM4-BT). Only the frequency deviation of the first mode is slightly higher than 1 % (Table 6). The MAC criterion presents values also higher than 85% except for mode 8 (0.42), which is probably due to unexpected modal displacement in the extracted mode shape (Fig. 3-j). The modal displacements of the measured mode shape at the second level have a larger amplitude than the others. In addition, we note an anomaly for a node at the top of the bell tower (Fig. 3-j). These observations may come from either an experimental anomaly (higher order modes being more difficult to identify) or a more complex phenomenon that is not considered in the model.

### 5.3 Global updating of FEM4

FEM4-BT and FEM3-Nave exhibit the lowest frequency and mode shape errors (Table 6, column FEM4-BT and FEM3-Nave), and parameters seem to converge towards a unique solution. They are used to update an assembled model FEM4. All design variables of each sub-model FEM3-Nave and FEM4-BT are updated. Design variables related to material properties are assigned to narrow bounds defined by the best solution  $\pm \sigma$ . Because  $K_x$  and  $K_y$  are key parameters for the model assembling FEM4-BT and FEM3-Nave, they can move within larger bounds. The best model's modal parameters are summarized in Table 10. Modes are arranged in the correct order. Some of them exhibit a discrepancy lower than 0.01 % with experimental data. Only numerical mode 5 has a frequency error higher than 5 %.

Exp. mode			FEM4			
#	$f_{exp}$ [Hz]	#	$f_{num}$ [Hz]	$\Delta f$ [%]	MAC	
1	2.61	1	2.61	< 0.01	0.98	
2	2.92	2	2.92	< 0.01	0.92	
3	3.94	5	3.72	5.58	0.67	
4	4.96	9	4.85	2.22	0.75	
5	5.25	12	5.10	2.86	0.54	
6	5.82	14	5.86	0.69	0.84	
7	6.84	16	6.84	< 0.01	0.72	
8	8.55	18	8.53	0.23	0.44	

TABLE 10 – Modal parameters of the best updated model for FEM4 after calibration. Results are compared to experimental modes in terms of frequency ( $\Delta f = \|f_{num} - f_{exp}\|/f_{exp}$ ), mode ranking (#), and MAC.

Density [ $kN.m^{-3}$ ]			Young's Modulus [MPa]			Lateral stiffness [N.m]			Poisson's ratio [-]		
Variable	Best sol.	$\sigma$	Variable	Best sol.	$\sigma$	Variable	Best sol.	$\sigma$	Variable	Best sol.	$\sigma$
$\rho_{BT-P4}$	28.9	0.23	$E_{BT-P4}$	1630	463	$K_x$	1.80e6	1.02e4	$\nu_{Nave}$	0.42	0.05
$\rho_{BT-P7}$	15.1	0.11	$E_{BT-P7}$	1120	623	$K_y$	9.08e6	1.32e4	$\nu_{Apse}$	0.24	0.09
$\rho_{BT-P9}$	16.7	0.32	$E_{BT-P9}$	620	14						
$\rho_{BT-fl0}$	8.05	0.62	$E_{BT-fl0}$	102	9						
$\rho_{Nave}$	31.1	0.23	$E_{Nave}$	2260	2.31						
$\rho_{Apse}$	15.2	0.26	$E_{Apse}$	1040	1.02						

TABLE 11 – Updated parameter of the model FEM4 expressed in terms of best solution (obtained from the minimal objective function F4) and standard deviation ( $\sigma$ ) of all solution (for  $S = 200$  particles).  $\rho$  is the mass density, E the Elastic Young's modulus, while the subscripts BT indicates bell tower, *fl0* indicates foer of the bell tower, P4, P7, P9 indicate the technique group associated with phase 4, phase 7 and phase 9 respectively.

The distribution of the variables is narrow around the best solution. The density of the nave (Table 5 and Table 11) and the lateral stiffnesses between the nave and the bell tower (Table 7 and Table 11) are the parameters that presented higher variability.

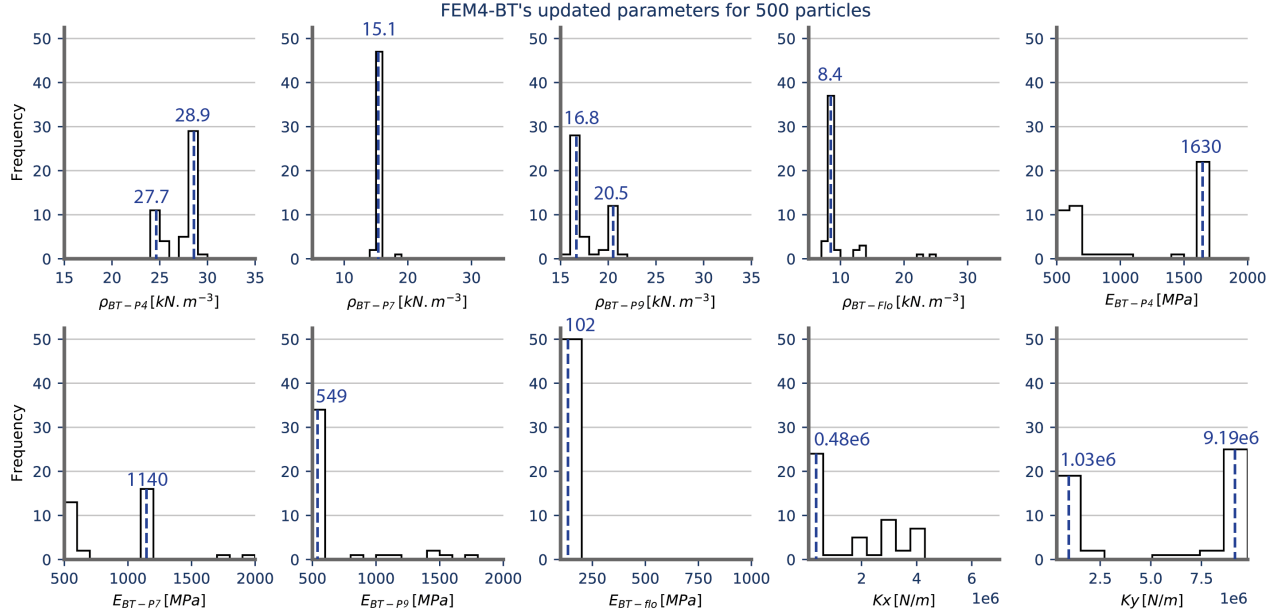


FIGURE 14 – Experimental mode shapes and numerical mode shape after calibration of FEM4.

## 5.4 Discussion

The results of the five models (FEM0-4) are discussed here to draw lessons from each strategy and identify a set of criteria and recommendations for the optimization of ancient masonry structures. Table 12 is a synthesis of the main features of the five models.

	FEM0	FEM1	FEM2	FEM3	FEM4
Parameters before SA	3	9	18	24	32
Parameters after SA	3	9	18	11	20
Objective function	F4	F4	F4	F2-F4	F2-F4
S	100	100	100	200	1000
exclusion criteria	mode paring	mode pairing	frequency deviation & updated parameters variability	frequency deviation updated parameters variability	-

TABLE 12 – Features of the 5 modeling strategies parameters (SA : Sensitivity Analysis).

### 5.4.1 Sensitivity analysis

Widely used in solving an inverse problem, sensitivity analysis is particularly effective in our case study for several reasons.

First, we use overdetermined models. The sensitivity analysis of the model parameters allowed to reduce the number of parameters of the FEM3 (11 parameters) and FEM4 (20 parameters) models. In the case of the 20-model parameters FEM4-BT, 1000 particles allow stabilizing the optimization around a minimum value of F2 and a global solution for the model parameters. Considering an average of 21 iterations for each optimization, this corresponds to 420000 forward modeling runs (modal analyses) to reach this result. This illustrates the interest in reducing the parameters from 32 to 20.

Secondly, this step is particularly efficient in helping in choosing the model parameters prescribed by the building construction history. This interest is, for example, confirmed in the FEM4 model (3 construction phases in the bell tower, modeling of an interface between the bell tower and the nave). The sensitivity analysis allows, however, to restrict the description of these phases to Young's modulus and the mass density.

We have selected parameters with a sensitivity coefficient greater than 5% rather than higher values (10% or 20%). This questionable choice allows us to give more weight to the construction history of the building rather than to a calibration criterion that will lead to a value averaging the constructive heterogeneities of the masonry.

Finally, the addition of stiffness at the interface between the tower and the ground is not retained because its influence on the modal frequencies is negligible in this case study. However, recent studies have demonstrated the influence of the ground on modal behavior (e.g., [Shabani et al. 2022](#)). Thus, to go further on this point, a characterization of the soil and appropriate modeling of the soil block and its interaction with the structure could be considered.

#### 5.4.2 The mode pairing technique criterion

The identification of mode pairs is the second criterion to be respected to ensure the coherence of the identified numerical modes. Redundancy of the mode pairs or the appearance of the numerical modes disorder leads to the exclusion of the modeling strategy. The FEM0 model is thus excluded because it presents both pathologies from the first bending modes (modes 1, 3, 5, and 6 in Tab. 4). It was shown that there is a poor correlation between the experimental and numerical modal deformation points at the interface between the bell tower and the nave (Fig. 11). This local analysis demonstrates the importance of modeling this interface. This echoes the late construction of the bell tower along the nave, which implies particular connection relationships between these two parts of the church.

The mode pairing technique criterion is not verified for the FEM1 model. The redundancy of one numerical mode with two experimental modes 5 and 6, underlines the importance of identifying enough higher-order modes to constrain the numerical modal basis better and thus the model parameters (Tab. 4). Note that this is a general limitation of the mode pairing technique criterion (even for the FEM4 modeling strategy) since it is impossible to identify all modes experimentally.

Only FEM2, FEM3, and FEM4 achieve this mode pairing criterion.

#### 5.4.3 Frequency deviation and low MAC values

The final frequency deviation of the best solution for FEM2 exceeds 5 % for modes 2 and 3, which is a significant error compared to the literature (tower optimization generally achieves frequency errors below 2%, e.g. [Standoli et al. 2021](#)).

For FEM3, the difference between numerical and experimental frequencies obtained with the best model remains too high ( $\Delta f \geq 5\%$  for mode 1 and 2 in Table 6) for the first two modes of vibrations, which is not acceptable for modes having the most important mass participation ( $\geq 70\%$  in X and Y direction).

FEM4's frequency optimization is particularly efficient since  $\Delta f \leq 0.01\%$  for modes 1, 2, and 7. Only mode 5 keeps a frequency optimization error higher than 5%. Although the optimization is acceptable, this last error questions the reflection to enhance the optimization process in excluding deficient mode or defining new objective functions.

This study benefited from a large number of points to identify the modal components. If this allows having a finer knowledge of the modal behavior, some singularities not included in the model can lead to a low value of the MAC. The mode shapes of the modes 4 and 5 present unexpected modal components, such as movement at one point of the base of the longitudinal wall and the three points along the windows (mode 4) and very complex shapes at the top of the longitudinal walls of the nave (mode 5). Some unexpected modal components may be related to the dynamic identification tests as discussed previously (at points W1, W2, W3 in Fig. 11). On the contrary, some others may be related to singularities that are not taken into account in the model. For mode 1, modeling the interface by adding stiffnesses improves the MAC values. For mode 5, the complex shape at the top of the longitudinal walls highlights an unidentified local behavior.

This experience opens up alternative perspectives. A first solution would be to exclude the nodes associated with identification faults since they have no physical meaning (the case of nodes W1, W2, and W3). A second solution would be to assign a lower weight coefficient to suspicious nodes or nodes with a misunderstood singularity in the framework of a new objective function.

This results in a low value in the model updating of those two modes.

#### 5.4.4 Variability of updated parameters



Masonry Typology	E [MPa]	Corresponding construction group
Disorganized irregular stone	690-1050	apse and P9 groups
Roughly cut stone with good texture	1500–1980	tower-P7 group
Stone blocks squared	2400–3200	group nave, tower-P4 group

TABLE 13 – Young’s moduli of Italian existing masonry categories (Table C8A.2.1, [delle Infrastrutture and dei trasposrti \(2009\)](#)) and the related construction group identified in Sant’Agata del Mugello.

The values and the variability of the optimized model parameters are now discussed. We recall that we assign a wide range of variation to the model parameters to test the consistency of the values obtained and, therefore, the modeling strategies. However, we stay aware that it remains difficult to judge the final values of the elastic masonry parameters since the ancient masonry is subject to complex phenomena related to the degradation process of the materials (some blocks and mortar of the church are exposed to aging for more than 10 centuries). We, therefore, restrict the discussion to the ranges of obtained values by comparing them to the values proposed by the Italian Building Code (Table C8A.2.2, [delle Infrastrutture and dei trasposrti 2009](#)), Italian Technical Standards for Structures (NTPC 2018). Three categories proposed by the Italian Building Code correspond to the masonry techniques identified in the church : *Disorganized irregular stone*, *Roughly cut stone with good texture*, and *Stone blocks squared*. The lower and upper bounds of Young’s modulus of the three selected categories from the Italian Building Code and the assumed corresponding construction technique groups are summarized in Table 13. The Italian Technical Standards for Structures proposes Young’s modulus between 600 and 3300 MPa, Poisson’s ratio between 0.01 – 0.45, and mass density between 15-20  $kN.m^{-3}$ . We also compared the updated model parameters to the values proposed by the Tuscan masonry database (Abaco delle Murature, [Boschi et al. 2017](#)). The database contains the results of experimental tests carried out on masonry panels of masonry buildings located in the Tuscany region. The database contains both qualitative descriptions of the masonry and quantitative description of the mechanical characteristics. Table ?? summarizes Young’s moduli ranges of tested masonry panels comparable with Sant’Agata’s construction techniques regarding qualitative description (masonry geometry, etc). The minimum, maximal, and mean values of Young’s moduli are reported in the Table.

For FEM2 (Table 5), the Poisson’s ratios are all consistent with the Italian Technical Standards for Structures (between 0.01 – 0.45). For the tower-P4 group, the mass density is consistent with the expected value (between 15 and 20  $kN.m^{-3}$ ). Since the tower-P4 group could be associated with the class *Stone blocks squared* of the Italian Building Code, the updated Young’s modulus is smaller than expected, even when compared with the regional Tuscan database. For the tower-P7 group, the mass density is too small, but Young’s modulus is consistent with the expected values of the two databases. For the tower-P9 group, the mass density is smaller, and Young’s modulus is greater than expected. Young’s modulus of the nave is consistent, although the density of the nave is exceptionally high. Using particularly dense limestone can explain this (Fig. 2). The value of the material properties of the apse is also higher than expected. We also note an essential variability of the updated densities and Young’s moduli, which indicates the model’s difficulty in converging toward a unique solution. The variability of the results and the recurrent deviation from the classically expected values of the elastic parameters call into question the construction of the model.

For FEM3, the mass density of the bell tower (model as a monolithic part) depicts a higher value than expected but a consistent Young’s modulus. The values of the model parameters of the nave are again a little high but can again be explained by using this dense limestone. Therefore, the obtained values are also quite close to those obtained by the FEM2 model. The updated model parameters of the apse are also consistent with poor masonry.

In addition to the poor quality of the masonry, the still visible presence of cracks partly explains the shallow value of Young’s modulus. The lateral stiffness is more significant in the longitudinal direction than in the transverse one, as expected by the very high stiffness given by the longitudinal wall of the nave. We note a less critical variability of the model parameters. Although the optimization of the nave and the apse seems coherent, the values of the parameters of the bell tower are too important (we recall that the FEM3 model also had a too significant frequency deviation for modes 1 and 2). This demonstrates the limitation of this model.

For FEM4, all the updated mass densities are consistent with the expected value from Italian Technical Standards for Structures. The high mass density of the tower-P4 group is consistent with masonry with blocks of dense limestone with only a small quantity of mortar. Young’s modulus is smaller than the expected value from Table 13 but compatible with Young’s moduli of similar masonry panels in the Tuscany region (Table ??). This smaller value is, however, consistent with damaged masonry since the tower-P4 group suffered the 1542 and 1611 earthquakes,

which highly damaged the bell tower. The Young’s moduli of the tower-P7 group, the nave, and the apse are consistent with the three reference databases. The Young’s modulus of the tower-P9 group is, however slightly smaller than expected values.

The updated lateral stiffness  $K_x$  and  $K_y$  show again a stiffer value in the longitudinal direction of the nave compared to the transverse one. The difference is, however, higher than in the FEM3-BT case. FEM4-BT shows a weak connection between the bell tower and the nave in the transverse direction.

The good agreement of updated model parameters with the three reference databases shows the consistency of the model FEM4 even when considering a large input interval of the model parameters for the optimization process. The variability of the updated parameters is small, confirming that the FEM4 converges towards a unique solution when considering 1000 particles. Furthermore, the updated model parameters’ final value echoes the church’s construction history. The degraded values of Young’s moduli may be consistent with the seismic history of the church. Furthermore, the stiffness values of the lateral connections are consistent with the weak connection between the bell tower and the nave due to the late construction of the bell tower.

At this stage of the study, the FEM4 model seems to be the most representative of the church of Sant’Agata not only from a numerical point of view (it respects the established criteria) but also because the values of the parameters have a physical meaning related the construction building history.

## 6 Conclusion

It is well-established that optimizing a numerical model of ancient masonry buildings is challenging due to masonry’s heterogeneity, non-linearity, and progressive degradation. However, OMA-based model updating has been successfully used to investigate the dynamic and seismic response of different typologies of historical masonry constructions (Ribeiro et al. 2012; Shabani et al. 2022; Azzara et al. 2019; Limoge 2016). To go a step further, we propose that OMA-based model updating of complex masonry buildings should be preceded by a deep understanding of the historical evolutions of the building as proposed in the ICOMOS guidelines (Charter 2003). Such an analysis add helpful information on building techniques, asynchronous construction, and repair operation induced after extreme events, such as earthquakes.

The approach is illustrated through the case of Sant’Agata del Mugello. Its seismic history has been retraced using a stratigraphic analysis supported by historical information from archives (Montabert et al. 2020).

With this aim, the paper highlights the contribution of the building history analysis of the church of Sant’Agata del Mugello and its combination with vibration-based identification methods to create and update a FE model. Sensitivity analysis and an extensive investigation of the parameters are performed using the PSO technique to identify the relevant parameters to take into account in the inversion process.

Five FE models of the church with an increasing enrichment of information coming from the building history are tested. The FEM0 model is only based on the knowledge of the building geometry and is used as a reference model. The FEM1 model considers the late construction of the bell tower and the side chapels, using different material properties for these three structures. The FEM2 model uses a more detailed description of the construction phase in the bell tower (group *tower-P4*, *tower-P7*, and *tower-P9*). In the FEM3 model, the late construction of the bell tower of Sant’Agata is considered through the optimization of the rigidity at the interface of the bell tower and the nave. The FEM4 model combines the FEM2 (building techniques decomposition) and FEM3 (interface between the bell tower and the nave) models.

The optimization of the simple numerical model (FEM0) did not ensure the uniqueness of the numerical and experimental mode paring (redundancy of the first numerical mode), as well as the order of appearance of the modes (numerical modes 4, 5, 6 do not appear in the order imposed by the experimental modes). The progressive incorporation of the building techniques allows to respect for the order of appearance of the modes (FEM1) and then the uniqueness problem (FEM3). The final value and the significant variability of the model parameters of the FEM3 model lead us to a more complex model FEM4. Incorporating the construction techniques observed in the bell tower and modeling the interface between the bell tower and the nave reduces the value of the objective function to the lowest value. However, the high number of parameters significantly impacts the convergence criterion. Using 1000 particles ensures that the model converges to a single solution. The final value of the updated parameters depicts a physical meaning related to the church’s construction history. The lower part of the bell tower has a lower-than-expected Young’s modulus consistent with the damage induced during the 1542 earthquake to this first construction phase. The stiffness at the interface between the bell tower and the nave has a low value consistent with the late construction of the bell tower against the nave with no quoins.

Based on these results, we would like to draw attention to a few key messages. First, we show that an exhaustive investigation of the construction history of the historic building based on a stratigraphic analysis of the building

walls allows for identifying groups of construction techniques. This analysis, combined with a study of the historical archives, can inform on the asynchronous construction of certain parts of the structure and/or reconfiguration of the building due the aggressive events (past earthquakes, [Montabert et al. 2020](#)). This information constrains the hypotheses when modeling the connections and groups of building techniques sharing the same mechanical properties. At first order, the sensitivity of the numerical frequencies to the elastic parameters of the FEM2 and FEM4-BT models confirms the importance of taking this constructive history into account.

Second, modal parameters extracted from OMA are the base block for VBMU. The number of identified modes and the accuracy in the mode shape identification leads to the model updating when comparing experimental and numerical data. A larger quantity of modes allows for constraining the families of solutions efficiently. With this aim, the mode pairing technique is a discriminating step. In our case, the higher-order modes allowed us to constrain the order of appearance of the modes and their frequency deviation.

Third, this case study shows the importance of a sensitivity analysis of each parameter, even for the number of particles of the swarm. We recommend identifying the minimum number of particles to ensure a stable convergence of the objective function value and of the model parameters.

Fourth, we propose running the optimization process several times since the variability of the optimized parameters allows a critical judgment of the modeling strategy and the physical meaning of the results.

This work has also demonstrated some limitations that need to be addressed in future research. The variability of the optimized parameters for the chosen strategy (FEM4) raises questions about the uniqueness of the identified solutions. Identifying higher-order modes could allow for better constraining of the solution space. In the case of Sant’Agata del Mugello, 81 nodes have been installed, allowing us to obtain this resolution theoretically. In practice, identifying modes beyond 8 Hz is difficult by very noisy singular values at high frequencies and mode shapes that are challenging to interpret. This raises questions about the method’s limitations in the case of ancient masonry buildings. Additional local measurements (such as ultrasonic characterization, e.g., [Pallarés et al. 2021](#)) would be an alternative to constrain the elastic parameters better. Therefore, optimizing the nave’s mode shapes leads to relatively low MAC values. While the optimization can undoubtedly be improved, it is essential to note that this may also be due to the uncertainty of the ambient vibration survey due to environmental conditions (strong winds) during the June 2019 campaign.

However, this multidisciplinary optimization strategy opens many perspectives for studying historic masonry buildings. In the Mugello basin, there are other buildings with similar construction histories whose updated mechanical property values could be compared with Sant’Agata del Mugello by applying this methodology. This method could be extended to other types of old buildings elsewhere to test these limits.

Regularly subjected to seismic events, the optimized Sant’Agata del Mugello (FEM4) model will allow us to evaluate the church’s vulnerability or understand its seismic response to ancient earthquakes.

## Acknowledgments

The authors thank Dr. Flomin Tchawe Nziaha for debugging multiprocessing in the PSO code and Dr. Cédric Giry for discussing the results. We also thank Dr. Hélène Dessales and Julien Clément for their advice during the development of this research work and comments on an early version of the manuscript. We thank Dr. Andrea Arrighetti for the discussions about the results. The authors kindly thank the editor and the two anonymous reviewers whose comments help increase the manuscript’s quality. The authors warmly thank the community of Sant’Agata del Mugello for their moral and logistic support, particularly the major Federico Ignesti, Don Gianluca Mozzi, Marco Casati, Filippo Bellandi, Paolo Gucci, and Anna Bambi.

This work was funded by Ecole Normale Supérieure, Institut de Radioprotection et de Sûreté Nucléaire, and the program TelluS-ALEAS of INSU-CNRS.

## Références

- Arrighetti, A. (2015, 2015). Constructive and seismic history of the sant'agata del mugello parish church. In P. I. LM (Ed.), *reuso 2015. III congresso internazionale sobre documentacion, conservacion y reutilizacion del patrimonio arquitectonico y paisajistico*, Valencia - ESP, pp. 64–70. Editorial Universitat Politècnica de València. Contributo in Atti di convegno.
- Azzara, R., M. Girardi, C. Padovani, and D. Pellegrini (2019, February). Experimental and numerical investigations on the seismic behaviour of the san frediano bell tower in lucca. *Annals of Geophysics* 61 (Vol 61 (2018)).
- Bianconi, F., G. P. Salachoris, F. Clementi, and S. Lenci (2020). A genetic algorithm procedure for the automatic updating of fem based on ambient vibration tests. *Sensors* 20(11), 3315.
- Bonini, M., G. Corti, D. D. Donne, F. Sani, L. Piccardi, G. Vannucci, R. Genco, L. Martelli, and M. Ripepe (2016, June). Seismic sources and stress transfer interaction among axial normal faults and external thrust fronts in the northern apennines (italy) : A working hypothesis based on the 1916–1920 time–space cluster of earthquakes. *Tectonophysics* 680, 67–89.
- Boschi, S., S. Giordano, N. Signorini, and A. Vignoli (2017). Abaco delle murature della regione toscana. *Proceedings of the XVI Convegno Nazionale ANIDIS, Pistoia, Italy*, 17–21.
- Brincker, R., C. E. Ventura, and P. Andersen (2001). Damping estimation by frequency domain decomposition. In *Proceedings of IMAC 19 : A Conference on Structural Dynamics : februar 5-8, 2001, Hyatt Orlando, Kissimmee, Florida, 2001*, pp. 698–703. Society for Experimental Mechanics.
- CEA. Cast3m.
- Ceravolo, R., G. Pistone, L. Z. Fragonara, S. Massetto, and G. Abbiati (2016). Vibration-based monitoring and diagnosis of cultural heritage : a methodological discussion in three examples. *International Journal of Architectural Heritage* 10(4), 375–395.
- Charter, I. (2003). Principles for the analysis, conservation and structural restoration of architectural heritage. *Proceedings of the ICOMOS 14th General Assembly in Victoria Falls, Victoria Falls, Zimbabwe*, 27–31.
- delle Infrastrutture, M. and E. dei trasposrti (2009). Circolare 2 febbraio 2009, n. 617 istruzioni per l'applicazione delle «nuove norme tecniche per le costruzioni».
- DPCM, y. *Direttiva del Presidente del Consiglio dei Ministri per valutazione e riduzione del rischio sismico del patrimonio culturale con riferimento alle norme tecniche per le costruzioni, G.U. n. 47*.
- Eberchart, R. and J. Kennedy (1995). Particle swarm optimization in : Ieee international conference on neural networks. *Perth, Australia*.
- Friswell, M. and J. E. Mottershead (2013). *Finite element model updating in structural dynamics*, Volume 38. Springer Science & Business Media.
- Gentile, C. and A. Saisi (2007). Ambient vibration testing of historic masonry towers for structural identification and damage assessment. *Construction and building materials* 21(6), 1311–1321.
- Gentile, C., A. Saisi, and A. Cabboi (2015). Structural identification of a masonry tower based on operational modal analysis. *International Journal of Architectural Heritage* 9(2), 98–110.
- Gunaydin, M., S. Adanur, and A. C. Altunisik (2018). Ambient vibration based structural evaluation of reinforced concrete building model. *Earthquakes and Structures* 15(3), 335–350.
- Hassan, R., B. Cohanin, O. De Weck, and G. Venter (2005). A comparison of particle swarm optimization and the genetic algorithm. In *46th AIAA/ASME/ASCE/AHS/ASC structures, structural dynamics and materials conference*, pp. 1897.
- ICOMOS (2003). Principles for the analysis, conservation and structural restoration of architectural heritage. In *Rap. tech., 14th General Assembly of ICOMOS*.
- Jaishi, B. and W.-X. Ren (2007). Finite element model updating based on eigenvalue and strain energy residuals using multiobjective optimisation technique. *Mechanical systems and signal processing* 21(5), 2295–2317.

- Kayashima, K., T. Doi, R. Yamasaki, and K. Imai (2017, dec). Long-axis ultrasonic images of the pediatric larynx and trachea with a cuffed endotracheal tube. *Anesthesiology* 127(6), 1016–1016.
- Limoge, C. (2016). *Méthode de diagnostic à grande échelle de la vulnérabilité sismique des Monuments Historiques : Chapelles et églises baroques des hautes vallées de Savoie*. Ph. D. thesis, Université Paris-Saclay (ComUE).
- Milani, G. and F. Clementi (2021). Advanced seismic assessment of four masonry bell towers in italy after operational modal analysis (oma) identification. *International Journal of Architectural Heritage* 15(1), 157–186.
- Milani, G., R. Shehu, and M. Valente (2017, August). Possibilities and limitations of innovative retrofitting for masonry churches : Advanced computations on three case studies. *Construction and Building Materials* 147, 239–263.
- Montabert, A. (2021). *Characterizing ground motion of historical earthquakes. Study of Sant’Agata del Mugello combining building archaeology, earthquake engineering and seismology*. Ph. D. thesis, Ecole Normale Supérieure (ENS), Paris, FRA.
- Montabert, A., H. Dessales, A. Arrighetti, J. Clément, M. Lancieri, and H. Lyon-Caen (2020). Tracing the seismic history of sant’agata del mugello (italy, tuscany) through a cross-disciplinary approach. *Journal of Archaeological Science : Reports* 33, 102440.
- Montabert, A., E. D. Mercerat, J. Clément, P. Langlaude, H. Lyon-Caen, and M. Lancieri (2022). High resolution operational modal analysis of sant’agata del mugello in light of its building history. *Engineering Structures* 254, 113767.
- NTPC, M. d. I. e. d. T. (D.M 17 gennaio 2018). Aggiornamento delle norme tecniche per le costruzioni. *Suppl. Ordin. Alla “Gazzetta Uff. n. 42 Del 20 Febbraio 2018- Ser. Gen.*, 1–198.
- Pallarés, F. J., M. Betti, G. Bartoli, and L. Pallarés (2021). Structural health monitoring (shm) and nondestructive testing (ndt) of slender masonry structures : A practical review. *Construction and Building Materials* 297, 123768.
- Prashanth, N. and P. Sujatha (2018). Comparison between pso and genetic algorithms and for optimizing of permanent magnet synchronous generator (pmsg) machine design. *International Journal of Engineering & Technology* 7(3.3), 77–81.
- Ramos, L. F., L. Marques, P. B. Lourenço, G. De Roeck, A. Campos-Costa, and J. Roque (2010). Monitoring historical masonry structures with operational modal analysis : two case studies. *Mechanical systems and signal processing* 24(5), 1291–1305.
- Ribeiro, D., R. Calçada, R. Delgado, M. Brehm, and V. Zabel (2012, July). Finite element model updating of a bowstring-arch railway bridge based on experimental modal parameters. *Engineering Structures* 40, 413–435.
- Rodrigues, J. M. V. B. L. et al. (2005). Identificação modal estocástica : métodos de análise e aplicações em estruturas de engenharia civil.
- Rovida, A., M. Locati, R. D. Camassi, B. Lolli, and P. Gasperini (2016). Catalogo parametrico dei terremoti italiani (cpti15).
- Saccorotti, G., R. Bruni, M. Bonini, G. Corti, D. Keir, and F. Sani (2022). Recent seismic sequences and activation of normal fault systems in the mugello basin and surrounding areas (northern apennines, italy). *Frontiers in Earth Science*, 646.
- Salachoris, G. P., G. Standoli, M. Betti, G. Milani, and F. Clementi (2023, jan). Evolutionary numerical model for cultural heritage structures via genetic algorithms : a case study in central italy. *Bulletin of Earthquake Engineering*.
- Shabani, A., M. Feyzabadi, and M. Kioumarsi (2022). Model updating of a masonry tower based on operational modal analysis : The role of soil-structure interaction. *Case Studies in Construction Materials* 16, e00957.
- Shabbir, F. and P. Omenzetter (2014, sep). Particle swarm optimization with sequential niche technique for dynamic finite element model updating. *Computer-Aided Civil and Infrastructure Engineering* 30(5), 359–375.

- Standoli, G., E. Giordano, G. Milani, and F. Clementi (2021). Model updating of historical belfries based on modal identification techniques. *International Journal of Architectural Heritage* 15(1), 132–156.
- Standoli, G., G. P. Salachoris, M. G. Masciotta, and F. Clementi (2021). Modal-based fe model updating via genetic algorithms : Exploiting artificial intelligence to build realistic numerical models of historical structures. *Construction and Building Materials* 303, 124393.
- Tarantola, A. (1987, April). *Inverse Problem Theory : Methods for Data Fitting and Model*. Elsevier Science Ltd.
- Torres, W., J. L. Almazán, C. Sandoval, and R. Boroschek (2017). Operational modal analysis and fe model updating of the metropolitan cathedral of santiago, chile. *Engineering Structures* 143, 169–188.
- Tran-Ngoc, H., S. Khatir, G. D. Roeck, T. Bui-Tien, L. Nguyen-Ngoc, and M. A. Wahab (2018, nov). Model updating for nam o bridge using particle swarm optimization algorithm and genetic algorithm. *Sensors* 18(12), 4131.
- Valente, M. (2021, November). Seismic vulnerability assessment and earthquake response of slender historical masonry bell towers in south-east lombardia. *Engineering Failure Analysis* 129, 105656.
- Wang, D., D. Tan, and L. Liu (2018). Particle swarm optimization algorithm : an overview. *Soft Computing* 22(2), 387–408.